LunarWSN: A Wireless Sensor Network for In-Situ Lunar Water Ice Detection

by

Fangzheng Liu

B.S., Beijing Institute of Technology (2015)
M.S., Beijing Institute of Technology (2018)

Submitted to the Program in Media Arts and Sciences
in partial fulfillment of the requirements for the degree of

Masters of Science in Media Arts and Sciences

at the

MASSACHUSETTS INSTITUTE OF TECHNOLOGY

September 2021

Author . . . .
Program in Media Arts and Sciences
August 19, 2021

Certified by . . . .
Joseph A. Paradiso
Associate Academic Head
Alexander W Dreyfoos (1954) Professor of Media Arts and Sciences
MIT Media Lab

Accepted by . . . .
Tod Machover
Academic Head
Professor of Media Arts and Sciences
MIT Media Lab

LunarWSN: A Wireless Sensor Network for In-Situ Lunar Water Ice Detection

by

Fangzheng Liu

Submitted to the Program in Media Arts and Sciences
on August 19, 2021, in partial fulfillment of the
requirements for the degree of
Masters of Science in Media Arts and Sciences

Abstract

The future lunar sustainable habitation will be resource-intensive. Taking advantage of local resources on the lunar surface is the most effective way to reduce the cost and risk for future lunar missions. Water is one of the most important resources that can provide not only drinking water for crews, but also fuel for rockets and spacecrafts. To date, most of our knowledge of lunar water distribution is from remote sensing, which is vague (kilometer-scale resolution). More in situ measurements are indispensable to acquire meter-scale resolution knowledge of lunar water distribution. The current main force of in situ planetary explorations is a single high-cost rover that can provide merely a series of single-point measurements or a lander without mobility that can only measure surrounding areas. Neither rovers nor landers can work in dangerous areas where data of interest often exists.

Wireless Sensor Networks (WSNs) are a technology that is typically dedicated to collecting in situ sensing data from regions of interest. A WSN is composed of multiple sensor nodes that are relatively small, light, and easy to deploy. The sensor nodes are designed based on a variety of missions and distinctly different environments. In this thesis, we present a WSN sensor node designed for measuring the water content in lunar soil simulant. The sensor node is designed to be ballistically deployed from a rover or lander to regions of interest that might be unsafe for rovers or landers. The sensor nodes can create an expandable WSN, that we term *LunarWSN*. The Lunar-WSN sensor nodes can make simultaneous observations from multiple positions. Each node is a miniaturized, modular design, whose sensor payload can be customized to different scientific missions. After anchoring on the lunar surface, the sensor nodes can localize themselves, set up a wireless communication network, and start the sensing operation — the measurements of permittivity of the lunar soil, which infers water content.

Thesis Supervisor: Joseph A. Paradiso
Title: Alexander W Dreyfoos (1954) Professor of Media Arts and Sciences

This thesis has been approved by the following committee members:

Advisor . . . .
Joseph A. Paradiso
Associate Academic Head
Alexander W Dreyfoos (1954) Professor of Media Arts and Sciences
MIT Media Lab

Reader . . . .
Jeffrey A. Hoffman
Professor of the practice
Co-director, Human Systems Lab
Department of Aeronautics and Astronautics
MIT

Reader . . . .
Martin S. Elvis
Senior Astrophysicist,
Center for Astrophysics
Harvard-Smithsonian

Acknowledgments

First, I want to thank my advisor, professor Joseph A. Paradiso, who is very supportive of this project and all my other work. I can not finish this project without the knowledge and suggestions offered by him. I am very grateful to become a member of the Responsive Environments group and the MIT Media Lab. This is the best place to pursue my space dream. I would like to thank my thesis readers, professor Jeffrey A. Hoffman from the MIT AeroAstro department, and Doctor Martin S. Elvis from Harvard-Smithsonian. Professor Hoffman is a successful NASA astronaut and he gave me a lot of great suggestions and feedback. Doctor Elvis shared with me a lot of thoughts about the future work of this project.

I additionally like to thank the members of Responsive Environments, who are the coolest labmates. Especially, I want to thank Brian Mayton, Mark Feldmeier, Artem Dementyev, and Patrick Chwalek. They helped me with solving a lot of hardware problems.

I want to thank my wife, Jing Qu, who gave up everything in China and came to the US with me. I can not accomplish anything without her support.

Last but not least, I want to thank my family and friends. It is their love and support that make me who I am today.

Contents

List of Figures

List of Tables

Chapter 1

Introduction

1.1 Motivation

Technologies that enable long-term, wide-range measurements on the lunar surface are crucial for future long-term human presence on the Moon, which is significantly resource-consuming. Water is one the most versatile resources that can serve as drinking water and potential fuel. Ferrying water from the earth is high-cost and unsafe. Taking advantage of local resources is a promising approach that helps to make long-term habitation possible. For now, our knowledge of lunar water deposits is restricted to orbital data and a single surface measurement [1]. More in situ measurements are essential to detect potential water deposits and confirm the remote sensing information [2]. Moreover, a lot of phenomena of interest are in hard-to-reach areas [3], such as Permanent Shadowed Regions (PSRs), craters with steep cliffs, caves with poor radio accessibility, rocky piles, etc. These areas are unsafe for current surface exploration systems, such as rovers, which have a history of wheel damage [4], and landers. Furthermore, there is increasing demand for more simultaneous data streams from multiple positions across areas of interest. This data is suitable for building models of dynamic phenomena [3]. Unfortunately, to date, rovers can only provide merely a series of single-point measurements. Without mobility, a lander can only investigate areas not far away from itself.

The WSN is a technology that can perform long-term measurements in areas of

interest and collect simultaneous data from multiple observations, and it is a game-changing technology for future lunar architecture [5]. Sensor nodes in a WSN can be small, light, low-cost, and easily deployed to hard-to-reach areas. A WSN can reduce the chance of failure through hardware redundancy and expendability. A set of sensor nodes can cover a large area in a short time with a proper deployment approach.

1.2 WSN in planet explorations

The WSN has been long used on earth for environmental monitoring and science inquiry [6–9]. These utilities show the intrinsic merits of the WSN, which give it extremely huge potential for in situ planetary explorations. A lot of research has been conducted to explore the applications of the WSN in planetary explorations. Research from European Space Agency (ESA) [10] divided the WSNs for space applications into five subclasses based on different utilities: (1) Microsensor Proximity Networks, which are in situ sensing networks with fixed nodes; (2) Intra-Spacecraft Proximity Networks, which are in situ sensing networks for the health of spacecraft and crews; (3) Inter-Vehicular Proximity Networks, which are in situ sensing networks with mobile platforms, such as low flying satellites, orbiters; (4) Extra-Vehicular Activity (EVA) proximity Networks, which are for data delivery during EVA; (5) Advanced Science Proximity Networks, which are composed of mobile sensor nodes. Our research falls into the first category. The PHALANX [3] presents a WSN in which the sensor nodes can be deployed by a cold-gas-propelled projectile launcher. The nodes are designed to expand the exploring capability of the rovers in unsafe areas. The sensor nodes can provide information about various environmental conditions, including volatiles, pressure, temperature, humidity, etc. The nodes can also serve as landmarks, communication relays, and illumination sources for a rover when it is doing subterranean reconnaissances in caves, lava tubes, etc. The ChipSat [11] is a miniature and lightweight (∼5g) spacecraft-on-chip system. Hundreds of Chip-Sats can be carried by an orbiter. When the orbiter finds a phenomenon of interest from orbit and needs in situ information, it will deploy hundreds of ChipSats to the

planetary surface to take ground measurements.

The ChipSat uses Commercial-Off-The-Shelf (COTS) sensors such as pressure sensors and magnetometers to study the planetary surface environment. The ChipSat shows a dual exploration architecture that combines remote sensing and in situ explorations. The Lunette [12] is a WSN that is composed of miniature landers for in-situ geophysical measurements. Each lander is equipped with a seismometer to collect seismic data for studying the internal of the moon. The landers serve as secondary payloads of an orbital spacecraft, and land on the lunar surface to create a lander network over an area of 10~20km. The Lunar Environment Monitoring Station (LEMS) is a compact instrument package [13]. With a mass spectrometer and a molecular electronic transducer, a LEMS can measure the lunar exospheric composition. The Space Wireless sensor networks for Planetary Exploration (SWIPE) [14] is another research effort that aims to monitor the planetary surface environment permanently. The sensor nodes in SWIPE are accurately deployed to desired positions through a rover, and the sensor nodes are designed for measuring radiation, temperature, illumination, and dust deposition.

1.3   In situ lunar water detection

The existence of water ice has been proved by decades of lunar explorations [15]. Most of the knowledge is from remote sensing [1]. As the only surface measurement for water ice detection, the LCROSS (Lunar Crater Observation and Sensing Satellite) uses an empty rocket to simulate the impact of a small-scale celestial body on the lunar surface [16]. With onboard science instruments, the LCROSS identified the existence of water from the impact location and debris plume. The LCROSS observations indicate an abundance of $\sim 5.6 \pm 2.9\%$ by weight (wt.%) of water [17]. However, the LCROSS took only a one-point measurement, and more information from ground measurements is essential for placing constraints on the abundance and distribution of water ice.

The VIPER (Volatiles Investigating Polar Exploration Rover) is one of many

efforts aimed at determining the distribution and composition of lunar water ice through in situ measurements. The VIPER is a robotic rover equipped with a drill, a neutron spectrometer (NS), a near-infrared (NIR) volatile spectrometer, and a mass spectrometer. The VIPER will analyze the water ice on the surface and subsurface at varying depths and temperature conditions [18]. By measuring the energy of neutrons emitted from the lunar soil, the NS can detect the existence of hydrogen, which implies the presence of water ice [19]. The NIR volatile spectrometer uses a lamp to illuminate the tailings pile as the rover drills into the subsurface. The NIR volatile spectrometer then leverages the reflectance spectroscopy of water ice to study its existence [20].

Another approach is leveraging a fundamental property of the lunar soil — dielectric permittivity, which can imply the existence of water ice [21, 25]. This has been used in many moisture measurement systems that determine water content in soil [22] or building materials [23, 24]. In [26], a commercial handheld LCR meter in conjunction with an Electrical Properties Cup (EPC) is used to measure the impedance spectroscopy of lunar/Martian soil simulants inside the cup. The results show that the impedance is strongly dependent on water content [26]. The Wireless Impedance Sensor Node (WISN) [27] is another research project to study the water content in lunar soil simulant by leveraging its dielectric permittivity. The WISN uses an impedance converter to measure the permittivity of the lunar soil simulant (JSC-1A [28]) with different water content (0%, 2%, and 5% by weight (wt.%)). The impedance converter feeds a sweeping-frequency (10kHz to 100kHz) AC signal to the lunar soil simulant through a pair of copper probes, which protrude into the simulant. The complex impedance of the simulant at different frequencies can be measured by the impedance converter. The permittivity of the lunar soil simulant can be inferred by leveraging the relationship between the permittivity and the complex impedance [29]. The measurement results showed the dielectric permittivity increases with higher water content. A WSN concept based on a WISN for future in situ lunar water ice detection is presented in [30].

1.4 LunarWSN concept

The LunarWSN is a WSN that is composed of miniature and modular sensor nodes. All sensor nodes can be deployed by a projectile launcher installed on a rover, lander, or dropped by a low-flying satellite. The LunarWSN also permits existing surface exploration systems, such as rovers and landers, to expand their inquiry capability by using massively redundant and expandable hardware. Each LunarWSN sensor node is small and lightweight. The sensor payloads of the sensor nodes can be chosen based on different scientific goals. Our current sensor payload refers to the WISN design and aims to detect the water content in lunar soil simulants by leveraging its dielectric permittivity. After being deployed on the lunar surface, the sensor nodes will localize themselves, set up a communication network, and start the scientific missions.

1.5 Literature structure

This thesis outlines the development of the LunarWSN. The rest of the thesis is organized as follows: Chapter 2 describes the structure of the system and the modular design of the node hardware. The design of each module is described in detail. Chapter 3 shows a series of tests in a lab environment for validation of the system, including wireless ranging, wireless communication, energy harvesting, and water content detection in lunar soil simulant. Chapter 4 discusses some possible deployment approach for the LunarWSN. Chapter 5 discusses the limitations of the current design, including the localization approach, energy harvesting strategy, the radio choice for wireless communication, etc. Some possible solutions according to these limitations are discussed. Finally, a program of future work is discussed for the improvement of the system performance.

Chapter 2

System

The whole system structure is shown in Fig. 2-1.
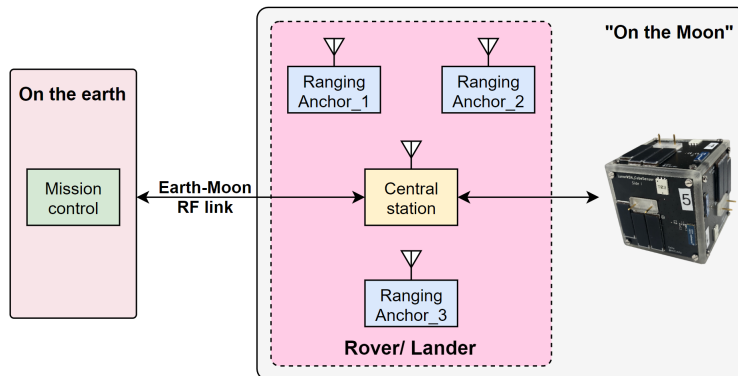
Figure 2-1: System block diagram of LunarWSN.

A LunarWSN sensor node localizes itself through wireless ranging with three fixed ranging anchors. A central station keeps a wireless connection with the LunarWSN and relays data back to a PC for real-time monitoring and control.

We made one node to represent nodes in the LunarWSN. A PC is used for mission control, and a serial port connection between the PC and the central station acts as the Earth-Moon RF link.

2.1 Design

2.1.1 Shape of the node

Different kinds of WSN nodes with different shapes are discussed in prior work. The PHALANX [3] proposed a projectile-like node design with tail fins. However, this aerodynamic design will not work well for stabilizing the node's orientation, since there is no air on the lunar surface. The fins take too much space — as much as the projectile body, which holds the sensor payload. We also considered a spherical shape design. However, most sensor payloads of interest are rarely spherical, which will cause a waste of the node's internal space. Moreover, after touching the lunar surface, a ball-shaped node can not provide a relatively deterministic landing and maybe rolling for a long distance, given the low gravity level on the moon. When we want to explore a crater, all spherical nodes may roll down from the cliff and crowd at the bottom. A tetrahedron shape node was also considered based on the SWIPE [14]. This design would require a deterministic landing orientation to guarantee sufficient antenna standoff above the surface. To realize a deterministic landing gesture, the nodes need to be put to the lunar surface in a specific orientation by a rover. This increases the complexity of the mission, and the nodes can not be deployed to some areas that are unsafe for the rover.

To face all the downsides mentioned, we designed a cubic-shaped node, which is shown in Fig. 2-2.

The node is a $5cm \times 5cm \times 5cm$ cube. All electronics can fit in the cube node, which guarantees an effective usage of the node's internal space. After touching the lunar surface, the cubic shape will stop the node from rolling for too long it should stop not far away from the planned location. Other components — such as solar panels, chip antennas — can be easily installed on the flat surfaces of the cube.
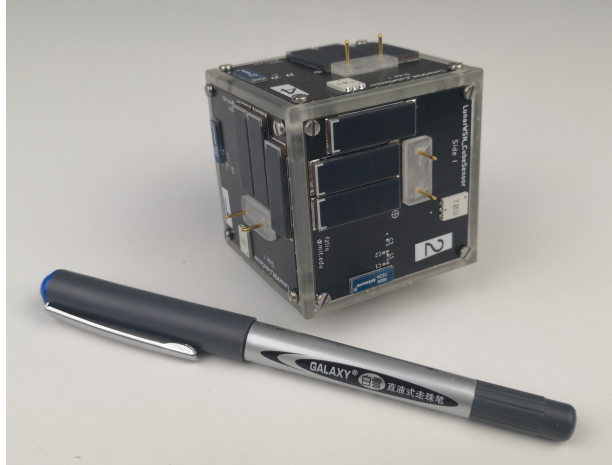
Figure 2-2: The cube-shaped node.
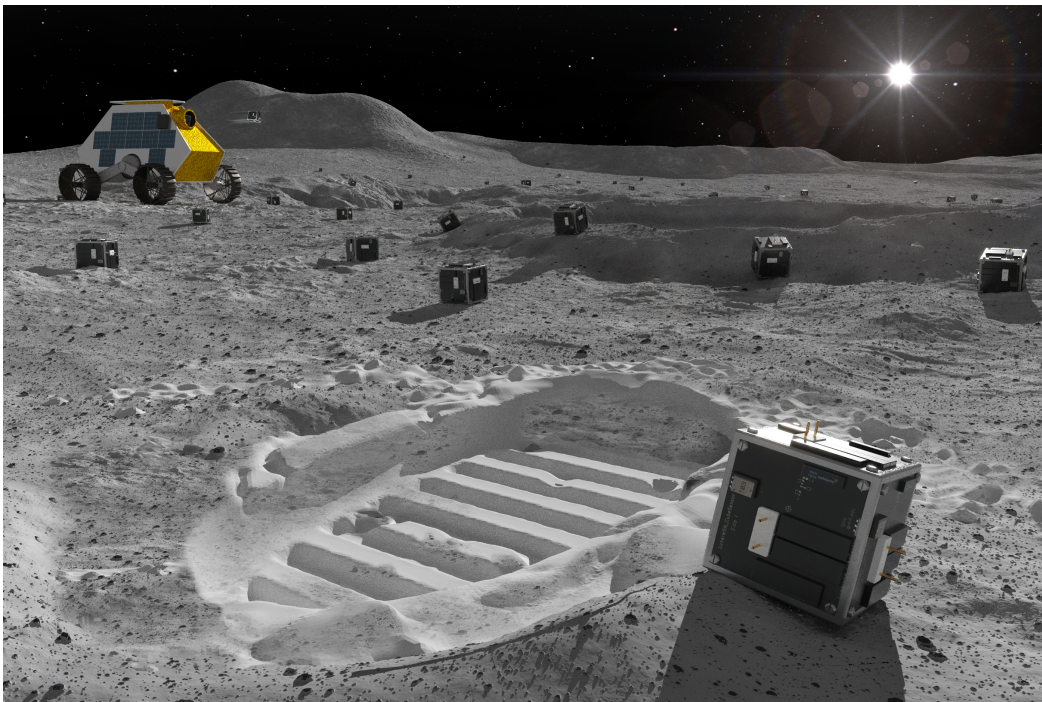
Figure 2-3: Artist rendering of LunarWSN working on the lunar surface.

2.1.2   Node Electrical System Design

We referred to the modular design of the CubeSat, which has a stack of PCBs inside the cube. Each board has a specific function and can be redesigned and replaced. The structure of the LunarWSN node is shown in Fig. 2-4.

The node is composed of six modules: (1) Antenna switch module, (2) Main Control Unit (MCU) module, (3) Sensor module, (4) Slow control module, (5) Power
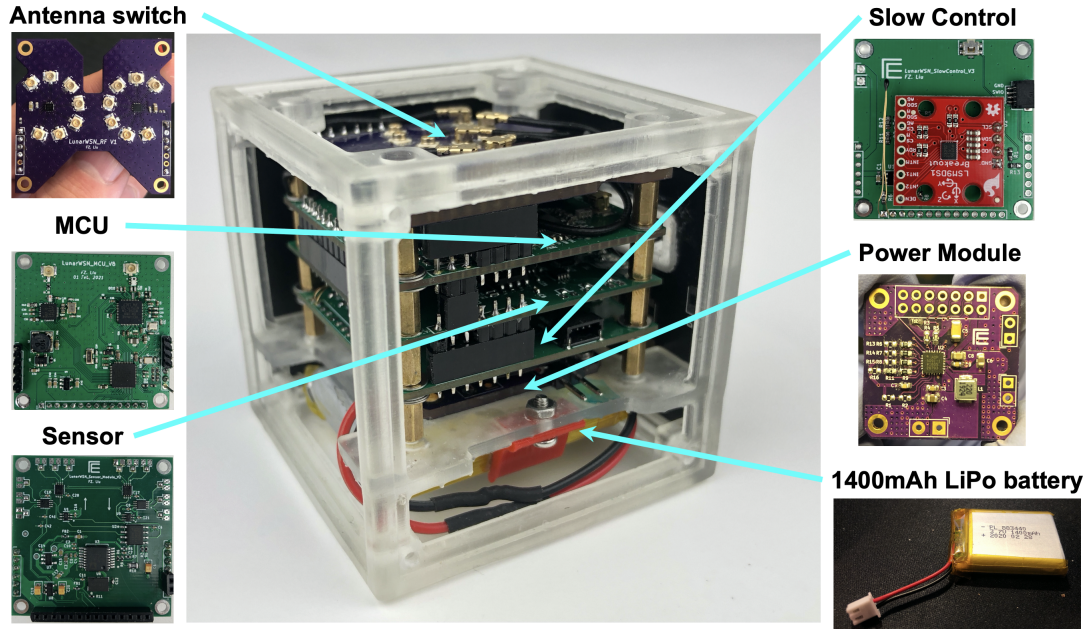
Figure 2-4: The structure of the node.

module & Battery, (6) Cube face. The system diagram is shown in Fig. 2-5.
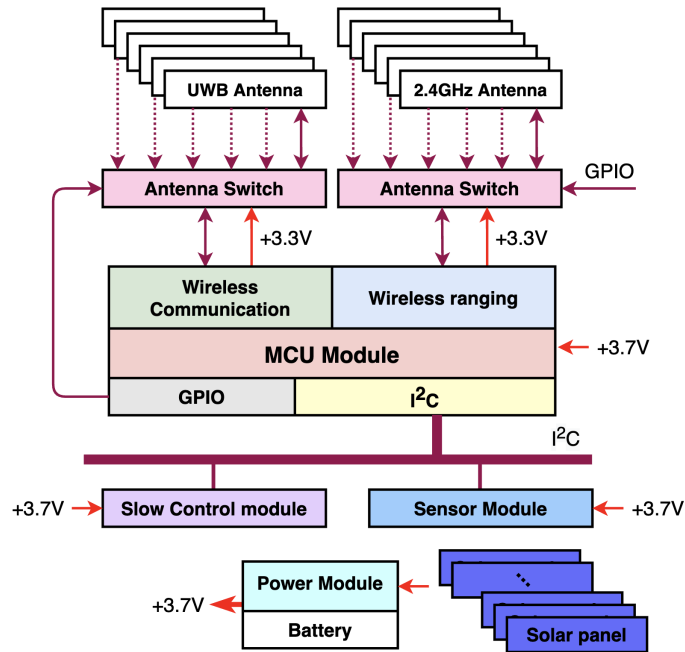
Figure 2-5: The node system diagram.

The MCU module is the main control module; it contains a wireless communication circuit and a wireless ranging circuit. The MCU module controls other modules

through different interfaces. The antenna switch module has two SP6T (Single-Pole-6-Throw) RF switch circuits that are responsible for choosing the antenna that can provide the best RF connection for wireless communication and wireless ranging. The sensor module is an impedance converter, which can measure the complex impedance of the Material Under Test (MUT); other sensor modules can also ne designed for this architecture. The SlowControl module is responsible for collecting House Keeping (HK) data, including internal temperature and battery voltage. The node is self-powered, and can harvest energy through solar panels on each side of the node when illuminated. The power module has a Maximum Power Point Tracker (MPPT) circuit that can harvest the most energy from the solar panels. There is a 3.7V Lithium Polymer (LiPo) battery for storing energy harvested. Detailed descriptions of each module are reported as followed.

MCU module

The MCU module is the core of the node. It performs the wireless communication, wireless ranging, and controls other modules through different interfaces (GPIO, I^{2}C, and SPI). The MCU module is shown in Fig. 2-6a. The circuit diagram is shown in Fig. 2-6b.
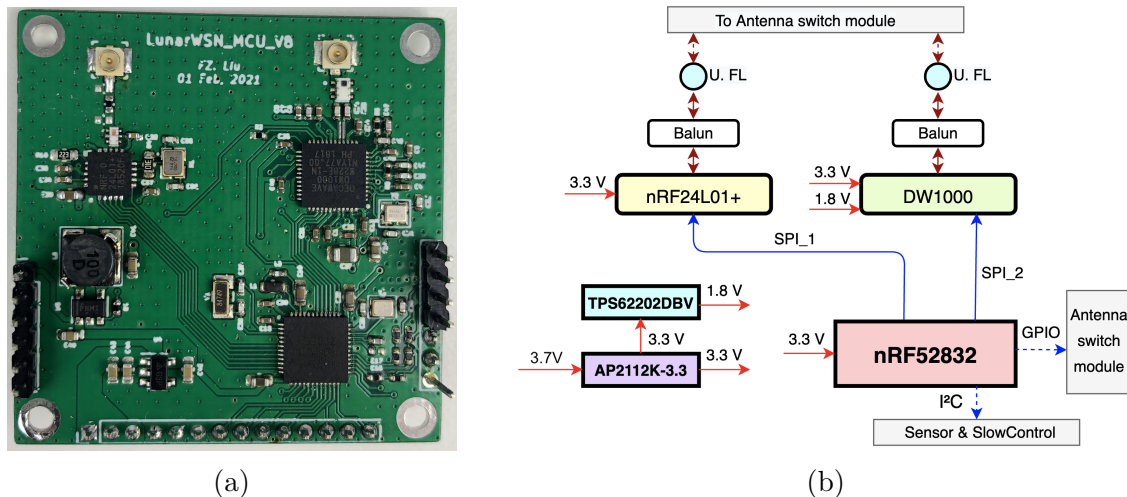

<div align="center">(a)   (b)</div>

Figure 2-6: (a) MCU module. (b) MCU module hardware diagram.

The main processor is a nRF52832 chip, which has a 64 MHz ARM Cortex-M4F

core [31]. The wireless communication is realized through a nRF24L01+ circuit, and the wireless ranging is realized through a DW1000 circuit. The nRF24L01+ is a single-chip low power 2.4GHz transceiver with an embedded baseband protocol engine (Enhanced ShockBurst [32]). The nRF24L01+ uses a frequency band at 2.4-2.4835GHz. The DW1000 is a multi-channel transceiver based on Ultra Wide Band (UWB) radio communications, and allows very accurate time-stamping of messages as they leave from and arrive at the transceiver [33]. The time stamp is the most important information we use to realize the wireless ranging.

Antenna switch module

The Antenna module chooses the antennas which can provide the best radio connection for wireless communication and wireless ranging. The module is composed of two SP6T RF switches (SKY13416-485LF [34]), which have a single power supply and can provide low insertion loss from 0.1 to 6 Ghz. The switches are controlled by the GPIO signal from the MCU module. The Antenna switch module and its diagram are shown in Fig. 2-7.

(a)   (b)
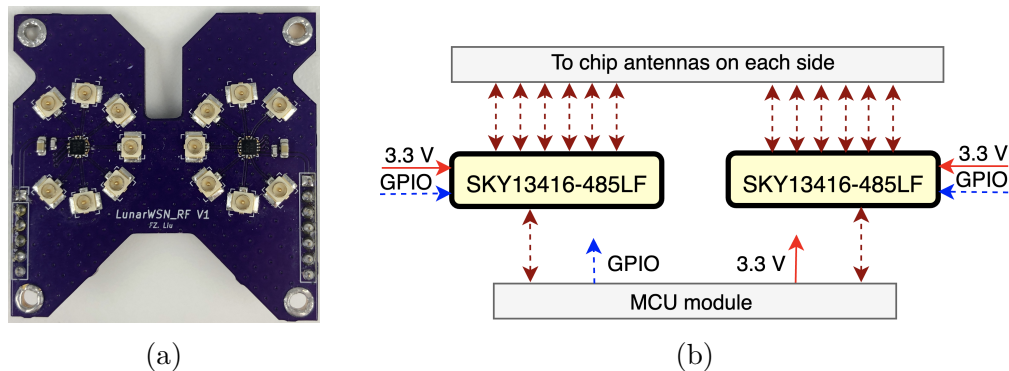
Figure 2-7: (a) Antenna switch module. (b) Antenna switch hardware diagram.

One SP6T switch chooses the antenna for the 2.4GHz wireless communication, and the other chooses antenna for the wireless ranging. The butterfly-shaped PCB leaves enough space for the coaxial cables that connect with the MCU module, Antenna switch module, and different antennas on each side of the node. The connections of the Antenna module are shown in Fig. 2-8.
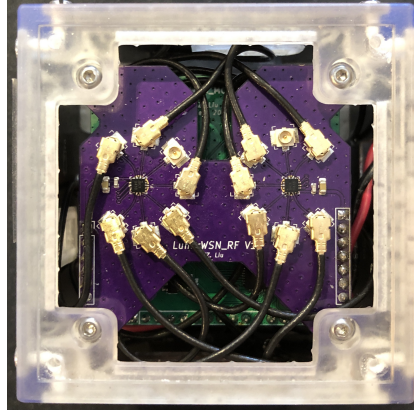
Figure 2-8: The Antenna switch connections.

Sensor module

The core component of the sensor module is an AD5933 chip, which is a high precision impedance converter that combines an on-board frequency generator with an Analogue-to-Digital Converter (ADC) and a Digital Signal Processor (DSP) [35]. The frequency generator allows a sample of MUT with a complex impedance to be excited with a known frequency, which is configurable. The response signal from the impedance is sampled by the built-in ADC, and a Discrete Fourier Transform (DFT) is performed by the built-in DSP. The DSP returns a Real (R) and Imaginary (I) data word at each frequency, and both are used for calculating the complex impedance of the MUT. There is a pair of sensor probes on each side of the cube for contacting with MUT at all six static orientations. Each pair of sensor probes is connected with the sensor module through a pair of coaxial cables, as shown in Fig. 2-9.

Besides the AD5933 circuit, the sensor module also includes two SP6T circuits, so they can choose which pair of sensor probes to use. Each SP6T circuit is made up of a SPDT (Single-Pole-Double-Throw) analog switch (ADG849) and two SP3T (Single-Pole-3-Throw) analog switches (TS5A3359DCUT). The hardware diagram is shown in Fig. 2-10.

27
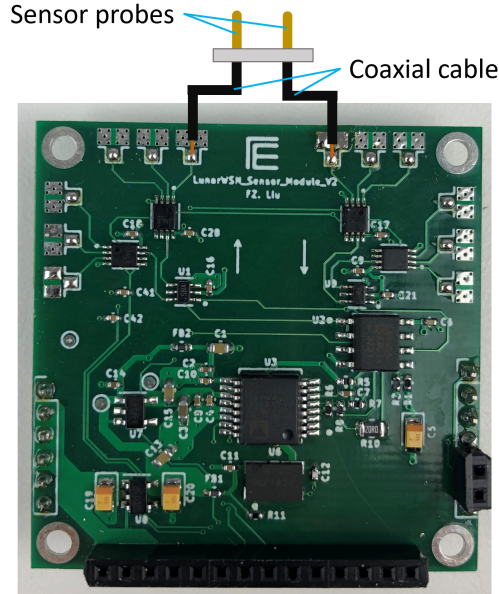
Figure 2-9: The Sensor module.
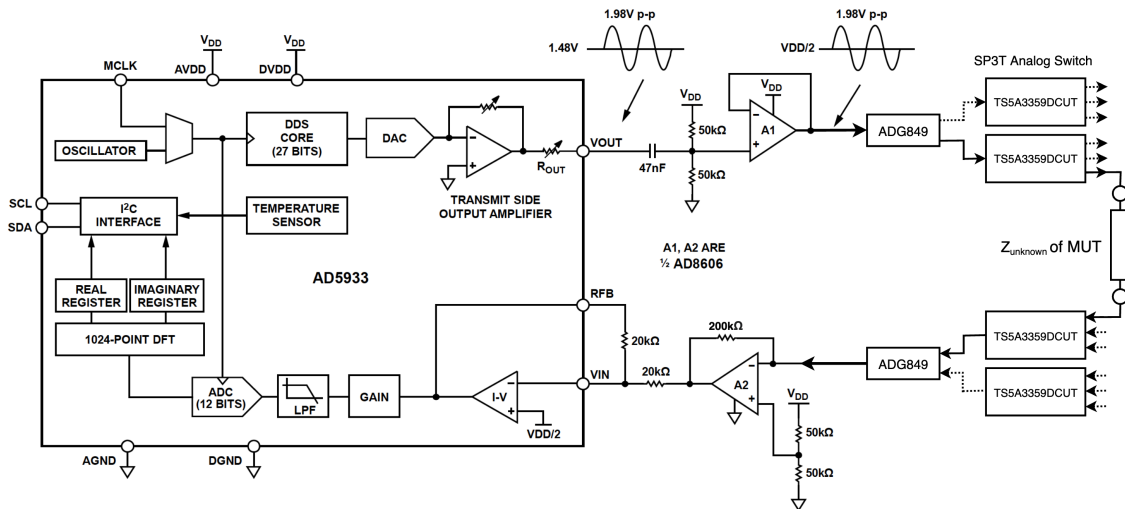
Figure 2-10: The Sensor module block diagram.

Slow Control module

The Slow control module (shown in Fig. 2-11) has a four-channel low-power ($150\mu A$) low speed (maximum sample rate: 860SPS) ADC (ADS1115 [36]) for collecting HK data that indicates the status of the node, including temperature (through thermistors) and battery voltage. The SlowControl module also includes a COTS IMU (Inertial Measurement Unit) sensor (LSM9DS1) module. The IMU sensor can measure the kinematic parameters (3-axis acceleration, 3-axis angular rate, and 3-axis

28

magnetic field strength) when the node is in flight and determine orientation of the node on the lunar surface. The Slow Control module also has a reset button for debug and a programming header for the Serial Wire Debug (SWD) of the nRF52832.
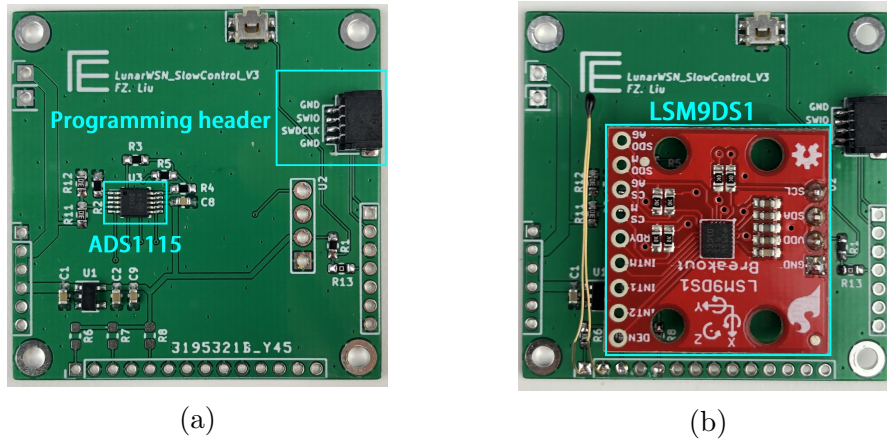
Figure 2-11: (a) The SlowControl module without the IMU (b) The SlowControl module with the IMU installed

Power module & battery

The power module is responsible for harvesting as much energy from the solar panels as possible and store it in a 1400mAh LiPo battery. The Power module has an AD5091 [37] MPPT chip. The Power module is shown in Fig. 2-12.
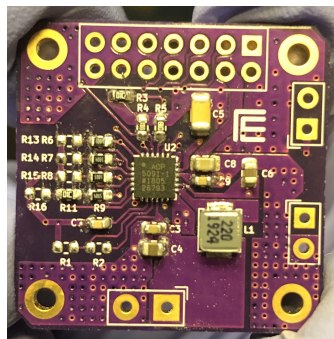
Figure 2-12: The Power module.

Cube face

The node has six faces and each one has a chip antenna (A5839 [38]) for wireless communication, an UWB chip antenna (AH086M555003-T [39]) for wireless ranging,

three solar panels (KXOB25_05X3F [40]), and a pair of copper probes for measuring impedance of the MUT. The structure of the cube side is shown in Fig. 2-13.

Figure 2-13: The structure of the sensor node side.

All components and PCBs that make up a sensor node are shown in Fig. 2-14.
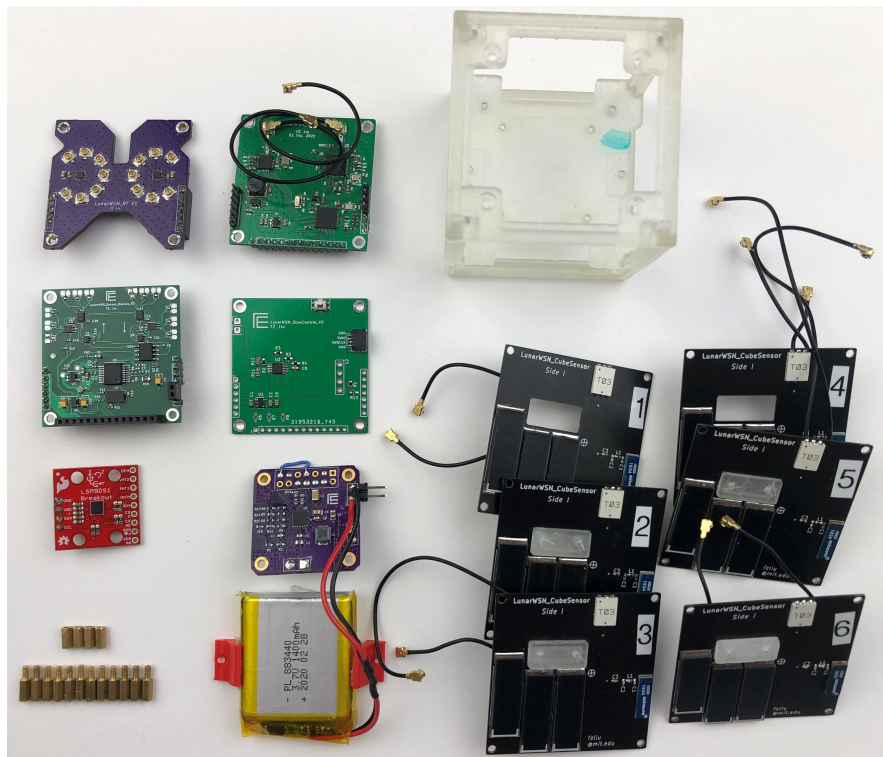
Figure 2-14: All components and PCBs that compose a node.

Each module can be redesigned and replaced based on the mission requirements and compatibility with other systems. For example, if the rover that relays the

data for the LunarWSN uses WiFi for wireless communication, then the nRF24L01+ circuit of the MCU module can be replaced by a WiFi circuit.

2.1.3   Ranging anchor and Central station

We also designed some external devices to support the node's operation. These are three wireless ranging anchors and a wireless communication central station.

The ranging anchors will be installed in known positions on a rover or lander, and they serve as coordinate references for the node's localization. Each ranging anchor has a DW1000 circuit for wireless ranging, and a COTS Arduino pro mini board. The Arduino board controls the DW1000 circuit and reports the distance measurement to a PC.

The central station is for relaying data from the node and forwarding commands to the node. The central station has an ATSAMD21G18 circuit and a nRF24L01+ module. The three ranging anchors and the central station are shown in Fig. 2-15.
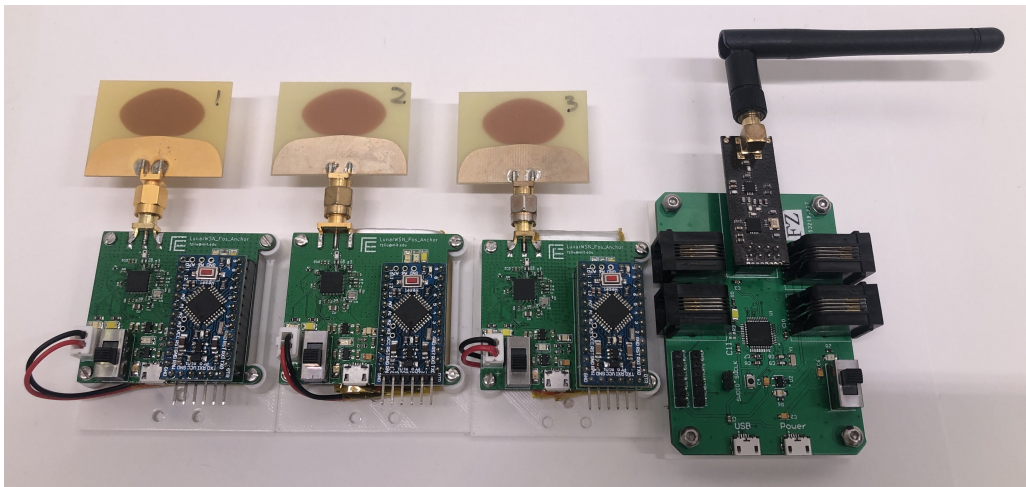
Figure 2-15: Three ranging anchors and the central station.

Chapter 3

System Validation

Multiple tests were conducted to validate the performance of the system, including wireless positioning, wireless communication, energy harvesting, and water detection.

3.1 Wireless positioning

The wireless positioning test is for testing the accuracy of the node localization.

Antenna delay calibration

The accuracy of the positioning is largely depend on the accuracy of the distance measurements between the node and each ranging anchor. The distances are measured by using Double-Sided Two-way Ranging (DS-TWR, shown in Fig. 3-1).
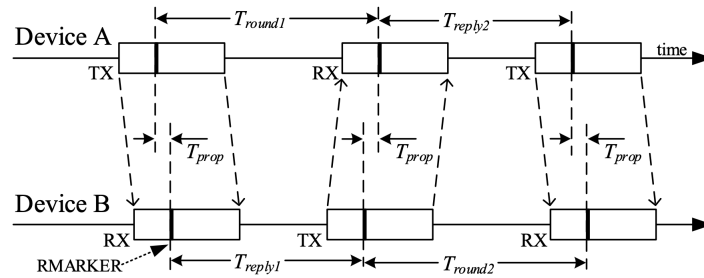
Figure 3-1: Double-sided Two-way ranging with three messages.

Where the T_{round1}, T_{round2}, T_{reply1}, and T_{reply2} are all calculated by using the time stamps of the messages. The distance is $d = T_{prop} \cdot c$ and $c = 299,792,458ms$. c is

the speed of light. The time-of-flight estimate, T_{prop}, is calculated as:

$$\hat{T}_{prop} = \frac{(T_{round1} \times T_{round2} - T_{reply1} \times T_{reply2})}{(T_{round1} + T_{round2} + T_{reply1} + T_{reply2})} \quad (3.1)$$

In order to measure distance accurately, we need to calibrate the antenna delay. This delay includes the RF propagation time in antenna and on PCB traces and will introduce huge errors into the positioning results.

The node was put at some known distances, with one side faced the three ranging anchors. Then the distances were measured. This process is repeated for each side of the node. 1000 measurements are taken at each distance for each side. The calibration test set-up is shown in Fig. 3-2a. Each anchor has a GUI for collecting and visualizing data, which is shown in Fig. 3-2b.
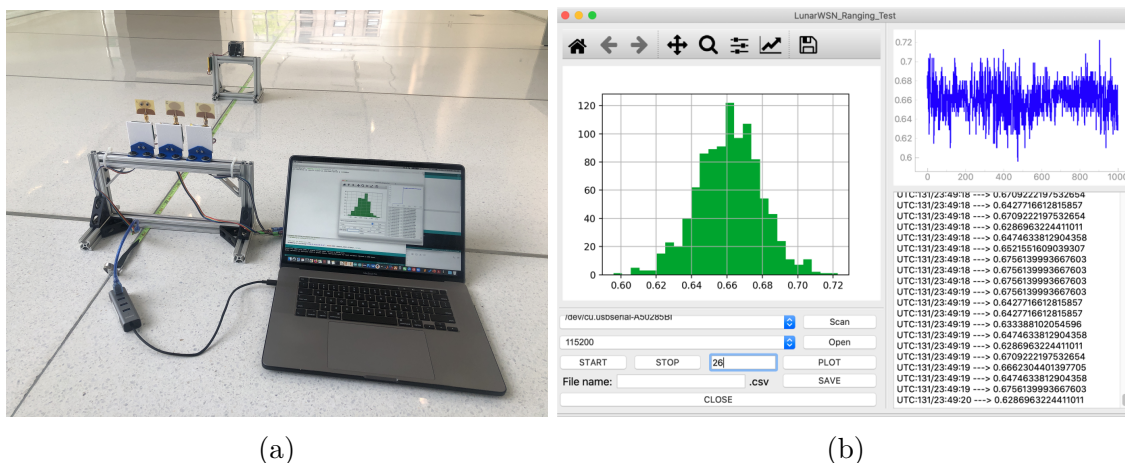
Figure 3-2: (a) Antenna delay calibration test set-up (b) GUI for antenna delay calibration.

The raw ranging data is plotted in Fig. 3-3.

To calibrate the antenna delay for each side, We did a function fit for the distance measurements. The least-squares fit is performed for the relationship of each side with each anchor as

$$y(x) = \sum_{m=1}^{M} a_m f_m(x) \quad (3.2)$$

Where $y(x)$ is the distance measurement result. From the raw data plot, the measurements and the real distance show a good linear relationship. So we set the f_m
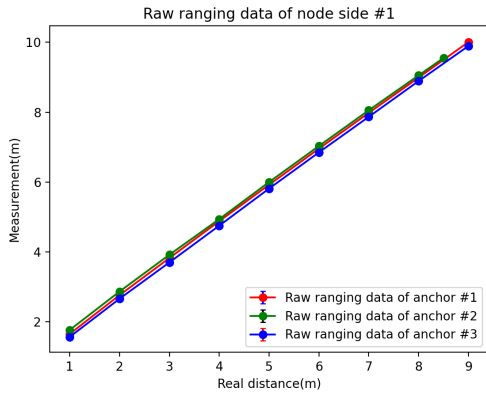
(a) Ranging test raw data of side 1
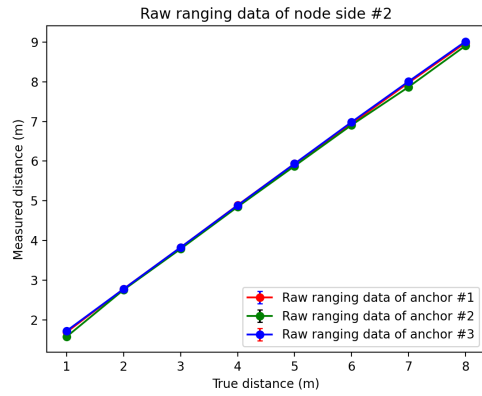
(b) Ranging test raw data of side 2
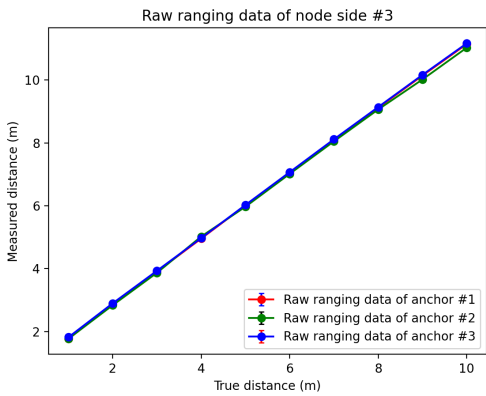
(c) Ranging test raw data of side 3
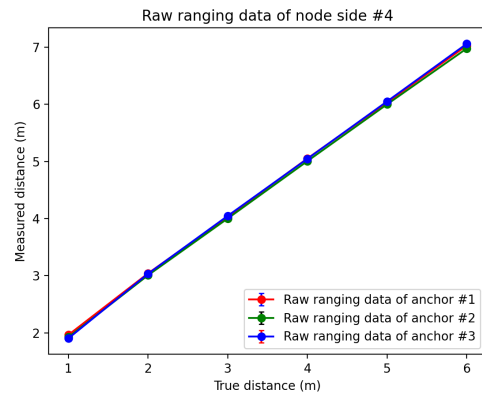
(d) Ranging test raw data of side 4
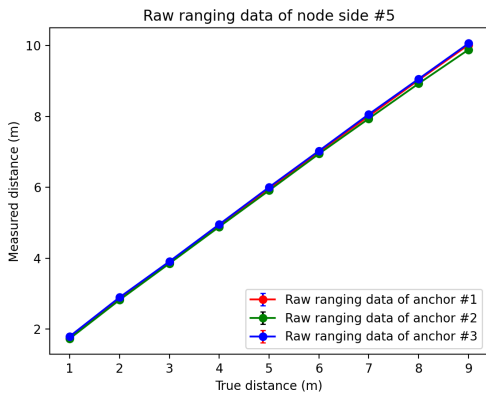
(e) Ranging test raw data of side 5
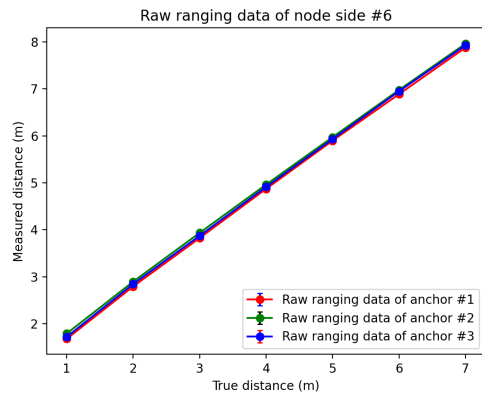
(f) Ranging test raw data of side 6

Figure 3-3: Ranging test raw data

polynomial terms accordingly, i.e., $f_m(x) = x^{m-1}$, and $M = 2$ (i.e., $y(x) = a_1 + a_2 x$).

Then the least squares fit can be written as a matrix problem

$$\mathbf{A}\vec{x} = \mathbf{Y} \tag{3.3}$$

Where

$$\mathbf{A} = \begin{bmatrix} 1 & x_1 \\ 1 & x_2 \\ 1 & x_3 \\ \vdots & \vdots \\ 1 & x_{N-1} \\ 1 & x_N \end{bmatrix}, \vec{x} = \begin{bmatrix} a_1 \\ a_2 \end{bmatrix}, \mathbf{Y} = \begin{bmatrix} y_1 \\ y_2 \\ y_3 \\ \vdots \\ y_{N-1} \\ y_N \end{bmatrix} \tag{3.4}$$

Where N is the number of different known distances. As the measurements exceed the unknown parameters (i.e., $N > 2$), we solve this problem by using Singular Value Decomposition (SVD). $\mathbf{A}$ can be decomposed as $\mathbf{A} = \mathbf{U}\mathbf{W}\mathbf{V}^T$, where $\mathbf{U}^T \cdot \mathbf{U} = \mathbf{V} \cdot \mathbf{V}^T = \mathbf{I}$. In terms of the SVD, the solution of $\mathbf{A}\vec{x} = \mathbf{Y}$ is

$$\vec{x} = \mathbf{V} \cdot \mathbf{W}^{-1} \cdot \mathbf{U}^T \cdot \mathbf{Y} \tag{3.5}$$

The results of each side to each anchor are shown in Table. 3.1.

The ranging errors after function fit are shown in Fig. 3-4.

Table 3.1: Least linear fit coefficients

Side	Anchor	a_1	a_2
	Anchor_1	0.6733257326	1.042246223
Side #1	Anchor_2	0.7684043444	1.040666942
	Anchor_3	0.6982909343	1.041394210
	Anchor_1	0.6961665990	1.040409771
Side #2	Anchor_2	0.6422219790	1.038763483
	Anchor_3	0.6963967939	1.044061858
	Anchor_1	0.7854582148	1.040270075
Side #3	Anchor_2	0.8114543100	1.027592233
	Anchor_3	0.8173791725	1.038592503
	Anchor_1	0.9967371577	1.008202360
Side #4	Anchor_2	0.9657017937	1.005857509
	Anchor_3	0.9440579322	1.022783063
	Anchor_1	0.7852475137	1.031363839
Side #5	Anchor_2	0.7824458804	1.019462664
	Anchor_3	0.8152146173	1.032294225
	Anchor_1	0.7088591498	1.030736629
Side #6	Anchor_2	0.8260241251	1.025229548
	Anchor_3	0.7518722758	1.031703219
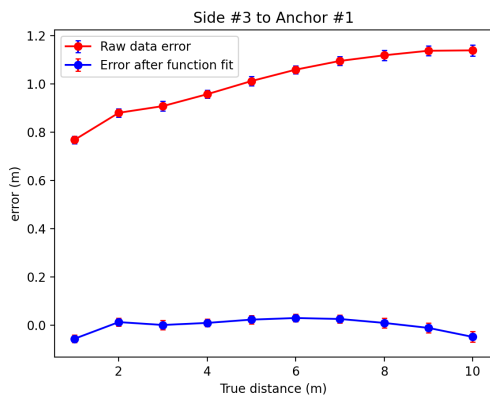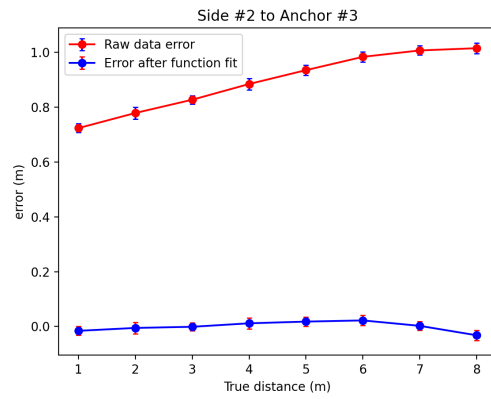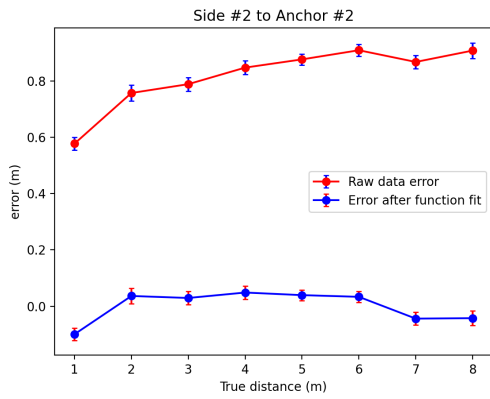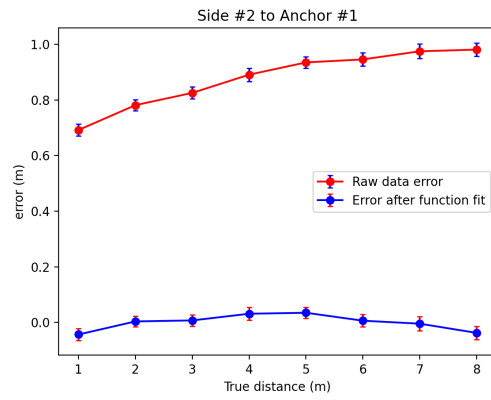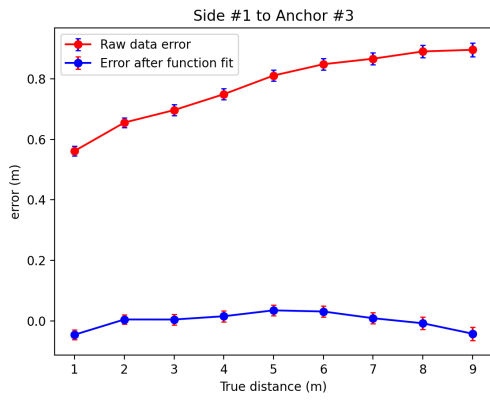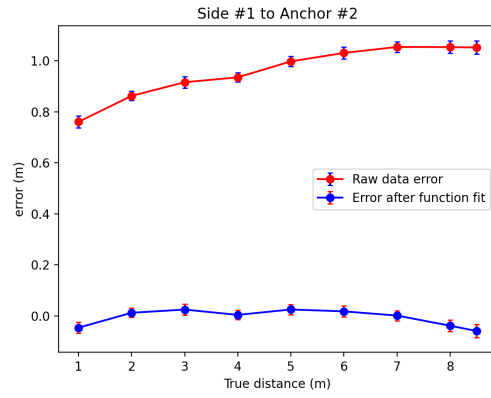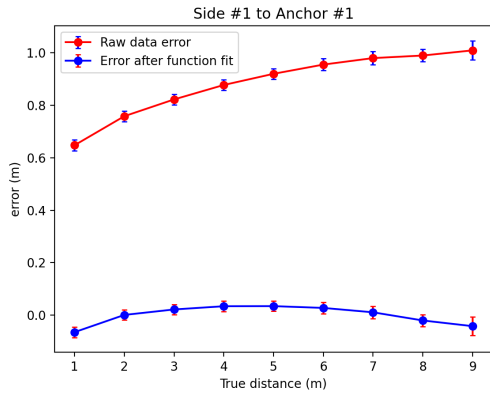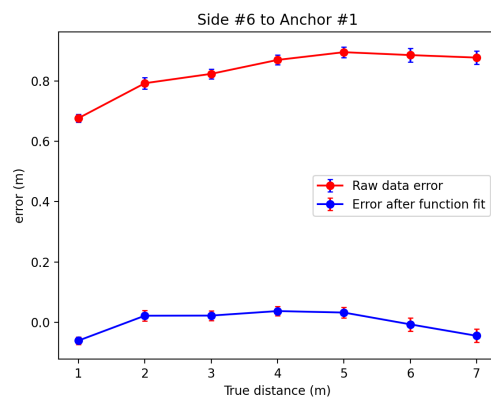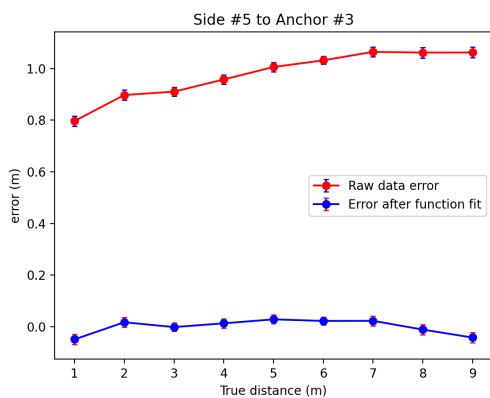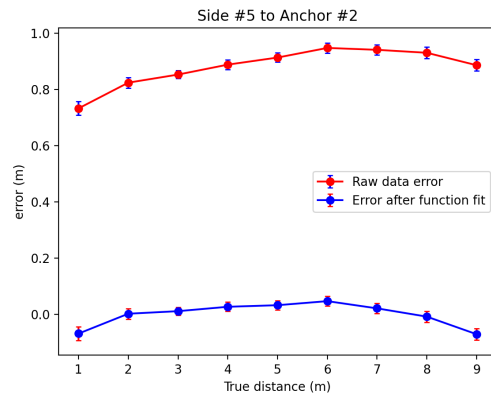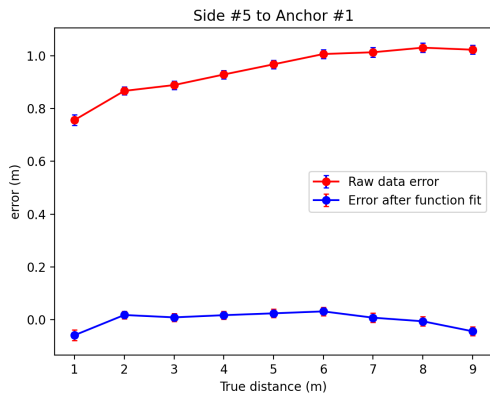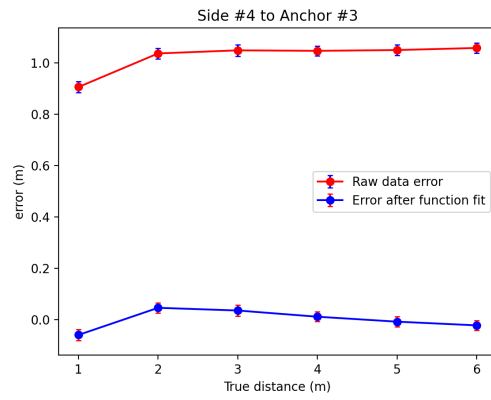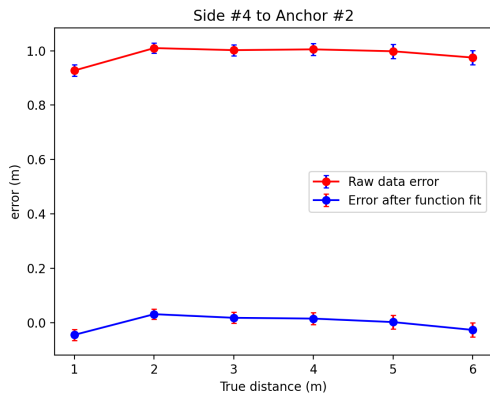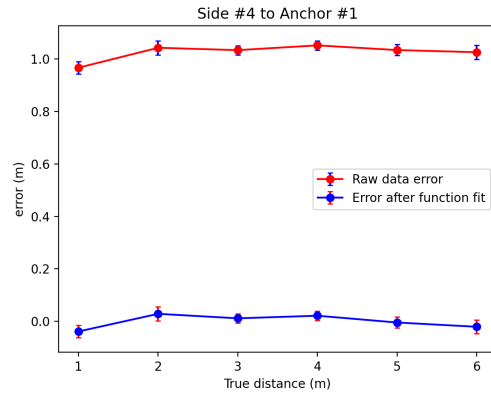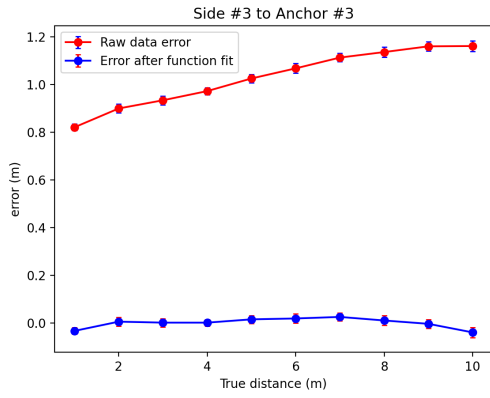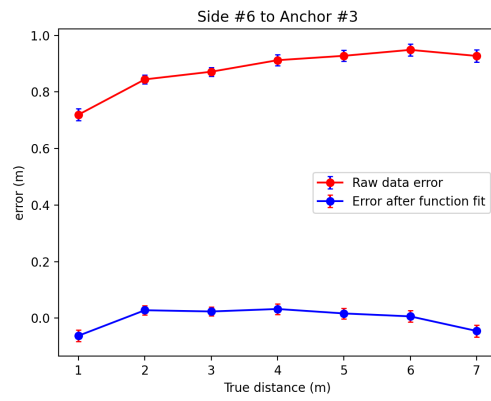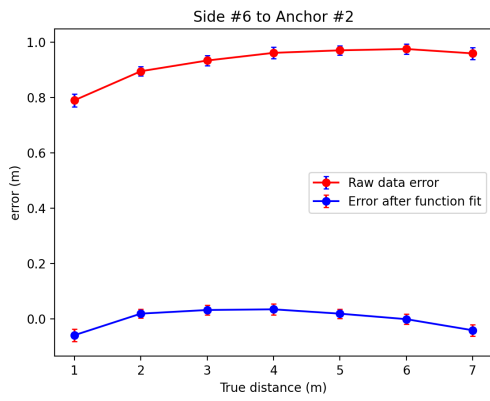
Figure 3-4: Ranging test error.

3.1.1 Localization test results

After antenna delay calibration, I set up the localization test in lobby of the MIT Media Lab, since there are grids that are made up of tiles on the floor, and each tile has a deterministic size ($4ft \times 8ft$). The deterministic size of the grids are used as positioning references. The test environment is shown in Fig. 3-5a. The ranging anchors and central station are installed on camera tripods, which are on deterministic positions, as shown in Fig. 3-5b, The node is randomly put on a joint of tiles on the floor, whose coordinate is known, as shown in Fig. 3-5c.

(a) The lobby of MIT Media Lab

(b) Ranging anchors and central station

(c) Node is put on a joint

Figure 3-5: Localization test setup in MIT Media Lab

The coordinates of the three ranging anchors are $P_i(x_i, y_i, z_i)$, where $i = 1, 2, 3$. The relative distance between the node and the ranging anchor i is d_i. Determination of the node's coordinate (x, y, z) is found by solving the following equations:

$$(x - x_1)^2 + (y - y_1)^2 + (z - z_1)^2 = d_1{}^2$$
$$(x - x_2)^2 + (y - y_2)^2 + (z - z_2)^2 = d_2{}^2 \qquad (3.6)$$
$$(x - x_3)^2 + (y - y_3)^2 + (z - z_3)^2 = d_3{}^2$$

Set the z of the ranging anchors to 0, i.e., $z_1 = z_2 = z_3 = 0$. As the node is on the ground, so the z of the node is $-h$, where h is the height of the ranging anchors.

Then equation 3.6 can be rearranged as:

$$x^2 + y^2 - 2x_1 x - 2y_1 y = d_1{}^2 - x_1{}^2 - y_1{}^2 - h^2$$
$$x^2 + y^2 - 2x_2 x - 2y_2 y = d_2{}^2 - x_2{}^2 - y_2{}^2 - h^2 \qquad (3.7)$$
$$x^2 + y^2 - 2x_3 x - 2y_3 y = d_3{}^2 - x_3{}^2 - y_3{}^2 - h^2$$

And equation 3.7 can be represented as:

$$\mathbf{AX} = \vec{b} \qquad (3.8)$$

Where

$$\mathbf{A} = \begin{bmatrix} 1 & -2x_1 & -2y_1 \\ 1 & -2x_2 & -2y_2 \\ 1 & -2x_3 & -2y_3 \end{bmatrix}, \mathbf{X} = \begin{bmatrix} x^2 + y^2 \\ x \\ y \end{bmatrix}, \vec{b} = \begin{bmatrix} d_1{}^2 - x_1{}^2 - y_1{}^2 - h^2 \\ d_2{}^2 - x_2{}^2 - y_2{}^2 - h^2 \\ d_3{}^2 - x_3{}^2 - y_3{}^2 - h^2 \end{bmatrix}$$

The coordinate of the node can be easily calculated by:

$$\mathbf{X} = \mathbf{A}^{-1}\vec{b} \qquad (3.9)$$

The user interface used for the test is shown in Fig. 3-6, and the test result is shown in Fig. 3-7.

42
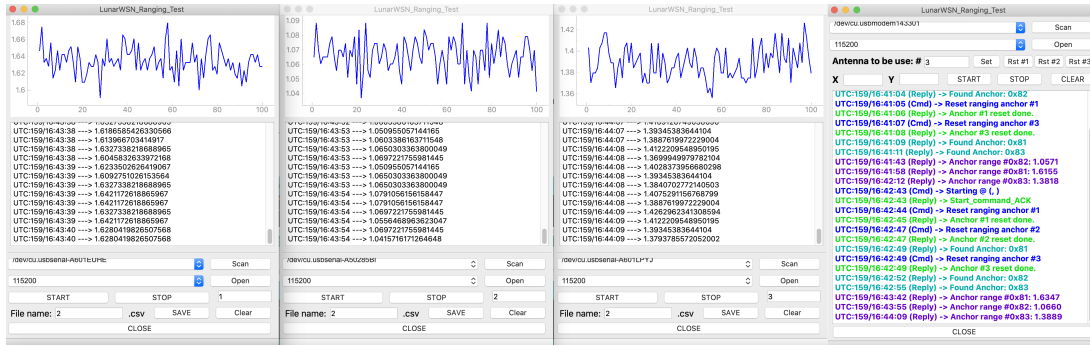
Figure 3-6: The GUI for the positioning test.
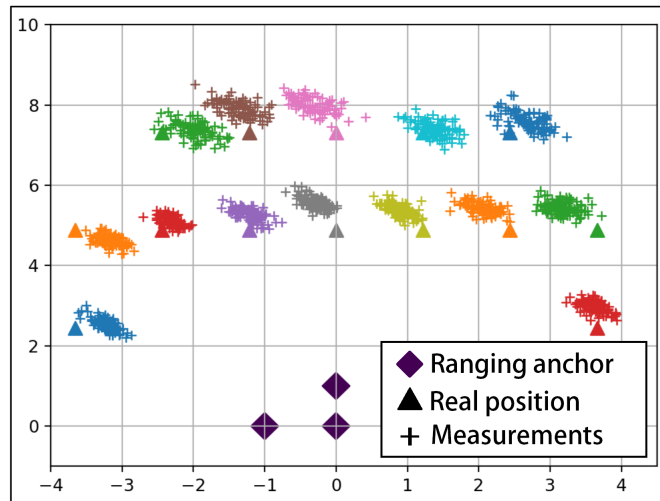
Figure 3-7: The localization test results.

3.2 Wireless communication

The communication is an important feature for the node, since keeping RF connection with other nodes or central station is essential for proper operation for the whole WSN. We tested the communication range of the node in the lobby of the MIT Media Lab. The node is put at some known distances with one side facing the central station. The node performs message exchanges with the central station by using the antenna on that side. The station will send a 10-byte-long message to the node and wait for the reply from the node. After the node receives the message from the central station, it will send the message back. If the central station didn't receive the echo from the node in 100ms or the message is wrong, the message exchange fails. This message exchange will be tested 500 times on each distance for each side of the node. Then

43

the successful exchange percentage is calculated for each side. The test setup and the GUI are shown in Fig. 3-8

(a)   (b)
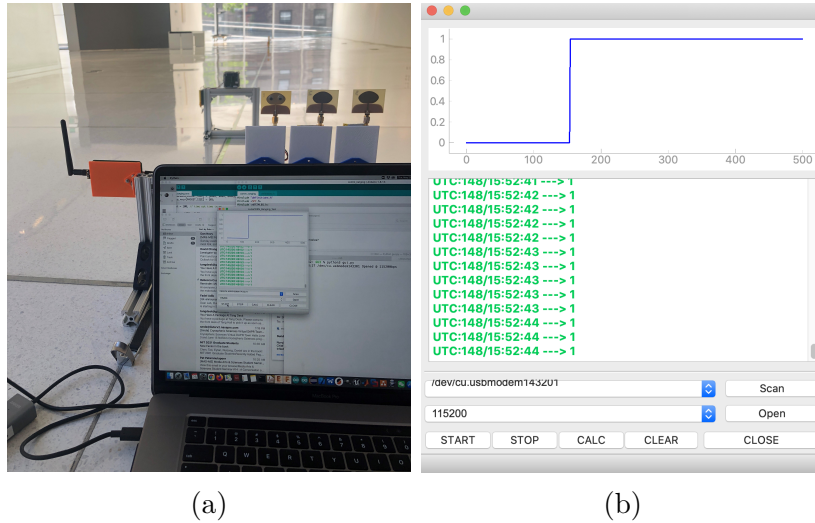
Figure 3-8: (a) Communication test setup (b) communication test GUI

3.2.1 Result

For successful communication percentage higher than 90%, the maximum communication range of the node is $7.5 \sim 8$m.

3.3 Energy harvesting

The node can harvest energy through the solar panels on each side to support long-term operation. To test the energy harvesting performance, the node is put under a solar irradiance condition that matches the average level on the lunar surface. The experiment setup is shown in Fig. 3-9a. Only the solar panels on one side are used. A high power LED is used for simulating the sunlight on the lunar surface, where the average daylight solar irradiance is $\sim 1368.0W \cdot m^{-2}$ [41]. The real irradiance of the high power LED is $170,900Lux$ ($\sim 1350.1W \cdot m^{-2}$), which is slightly lower than the average condition. The experiment setup diagram is shown in Fig. 3-9b.

The built-in ADCs of a $Feather\ M0$ board are used to sample the voltages of the
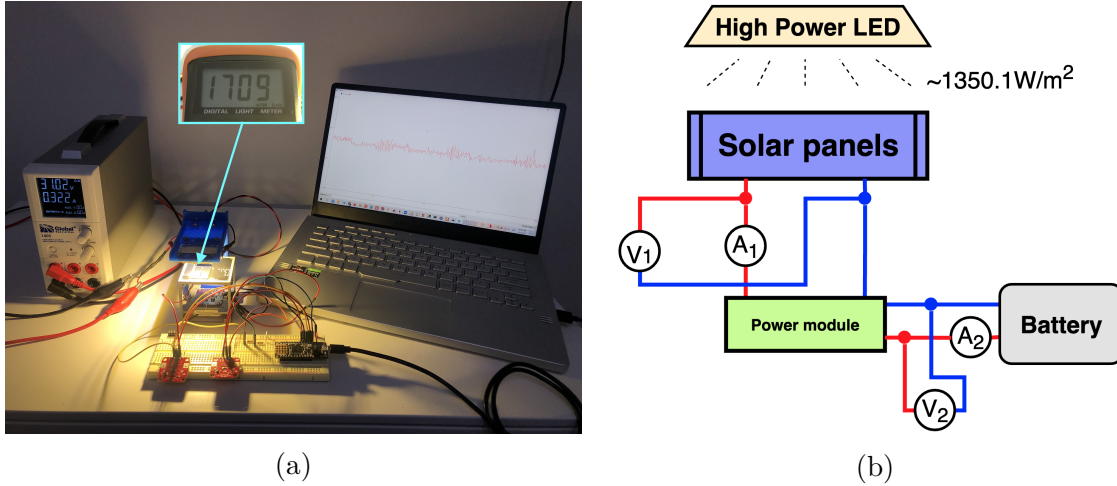
Figure 3-9: (a) Energy harvesting test setup (b) experiment diagram

solar panels (V_1) and the battery (V_2). Two current sensors (INA169 [42]) are used to measure the current of the solar panels (A_1) and battery (A_2).

3.3.1 Results

The solar power harvested is $P = V_2 \cdot A_2 \approx 18mW$, as shown in Fig. 3-10a. The small ripples in Fig. 3-10a are due to the periodic open-circuit of the power module to sample the open-circuit voltage of solar panels [37]. The power harvesting efficiency, which is the ratio between the power derived by the battery and the power output from the solar panels, i.e., $P = (V_2 \cdot A_2)/(V_1 \cdot A_1) \times 100\%$, is $\sim 83\%$, as shown in Fig. 3-10b.
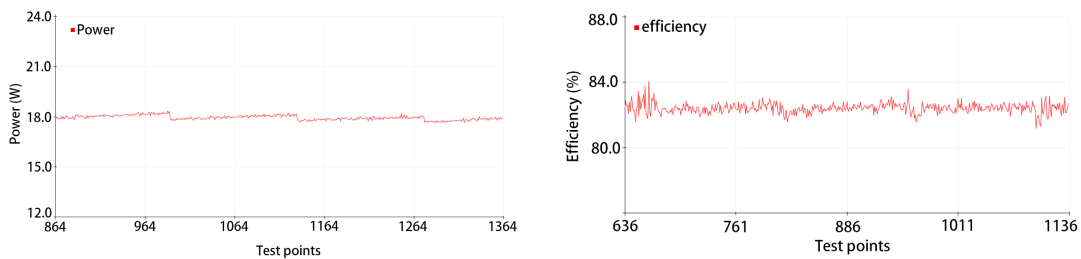
(a) Power harvested.

(b) Solar energy harvesting efficiency.

Figure 3-10: The power harvesting test results.

The estimated power consumption is shown in Fig. 3-11. The localization lasts 5s and operates only once. The node will wake up only once per minute, work for 10s,

and back to sleep for 50s. According to the power harvesting experiment results, the node can work for ∼8 days without any energy harvested. With power harvesting, the node can work for ∼21 days, which is longer than the lunar daylight, which is ∼14 days.
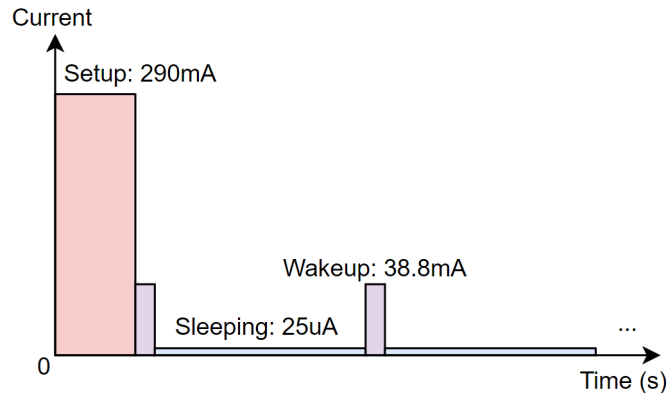
Figure 3-11: Estimated power consumption.

3.4   Water detection

The water detection performance was tested in a lab environment.

3.4.1   Sensor calibration

The sensor module injects a sweeping-frequency AC signal into the MUT (sands and lunar soil simulant with different water content). The response from the MUT is sampled by the built-in ADC of the AD5933, and a DFT is performed by a built-in DSP. The DSP returns a real (R) and an imaginary (I) data-word. Then the DFT magnitude is

$$Magnitude = \sqrt{R^2 + I^2}$$

To convert the *Magnitude* to impedance, it must be multiplied by a gain factor [35]. The gain factor at each frequency is scaled by the calibration with a known impedance in contact with the sensor probes, as shown in Fig. 3-12.
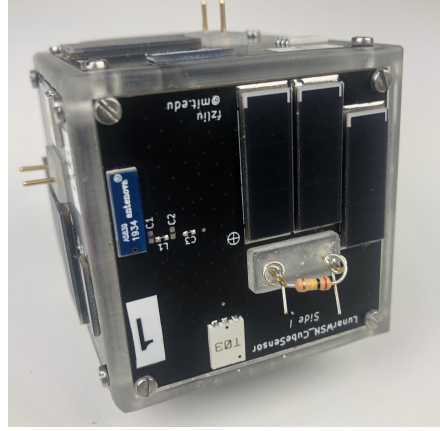
Figure 3-12: Sensor calibration with a 200kΩ resistor.

The gain factor at a single frequency is calculated by

$$Gain\ factor = \frac{(\dfrac{1}{impedance_{known}})}{Magnitude}$$

Then the measured impedance (Z) at that frequency is given by

$$Z = \frac{1}{Gain\ factor \times Magnitude}$$

We use a 200kΩ resistor for calibration and measured some known resistors; the results are shown in Fig. 3-13

The impedance phase θ is given by

$$\theta = tan^{-1}(I/R) - \theta_{system} \qquad \theta_{system} = tan^{-1}(I_{cali}/R_{cali})$$

The I_{cali} and R_{cali} are the data-word attained by the calibration with a known resistor. All phase angles need to be corrected instead of dividing the I with R directly. The correction depends on the sign of the I and R, as shown in Table. 3.2

Then the Real (Z_R) and Imaginary part (Z_I) of the complex impedance are given by

$$Z_R = Z \times cos(\theta) \qquad Z_I = Z \times sin(\theta)$$

The Real (ε') and Imaginary (ε'') part of the MUT permittivity is related with the Z_R and Z_I as [29]

47
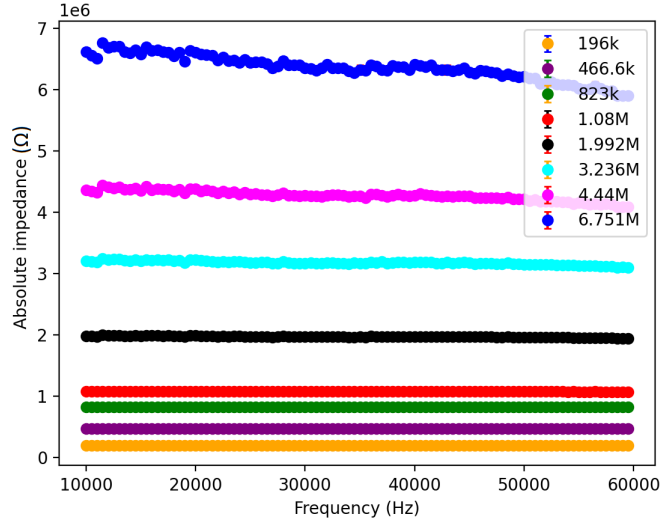
Figure 3-13: Responses of resistors after calibration with a 200kΩ resistor.

Table 3.2: Phase angle correction

R	I	Phase angle
Positive	Positive	$tan^{-1}(I/R)$
Negative	Positive	$\pi + tan^{-1}(I/R)$
Negative	Negative	$\pi + tan^{-1}(I/R)$
Positive	Negative	$2\pi + tan^{-1}(I/R)$

$$\varepsilon' = \frac{-Z_I}{g\omega\varepsilon_0(Z_R^2 + Z_I^2)}$$

$$\varepsilon'' = \frac{Z_R}{g\omega\varepsilon_0(Z_R^2 + Z_I^2)}$$

Where $g\varepsilon_0$ is a constant (the capacitance between the empty probes), and $\omega = 2\pi f$ (f is the frequency in Hz). The ε' is the parameter we use to infer different water content.

3.4.2 Results

The tests are divided into two phases. Both phases use deionized, ultrapure water (type I water [43]) to control the water content in the MUT (sands and lunar soil simulant). In our experiments, only the sensor probes on one side are used, and the test process and data processing (including calibration) for the others are exactly the

same.

Phase I — testing the sensor by using natural sands with different water content (Dry, 0.89%, 2.14%wt, 3.47%wt by weight (wt.%)) at room temperature (24°C). This is just for testing the function of the sensor and no further data processing is necessary, since lunar soil is different from sand. The sands are put into a plastic cup. The doped ultrapure water is pipetted into the sand, and the water and sand are mixed together by vigorous hand shaking. The sensor node is put into the cup after sensor calibration and the probes fully spike into the sands. The central station is installed on top of the cup to get a good wireless connection. The experiment setup is shown in Fig. 3-14. A custom GUI was designed to collect data, monitor and control the experiment, as shown in Fig. 3-15.
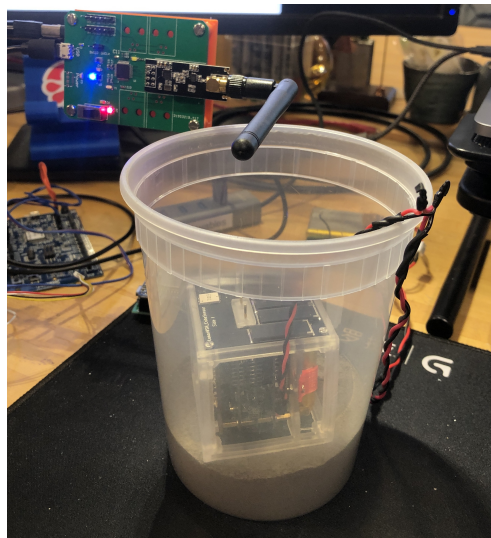
Figure 3-14: Water detection test setup with sands.
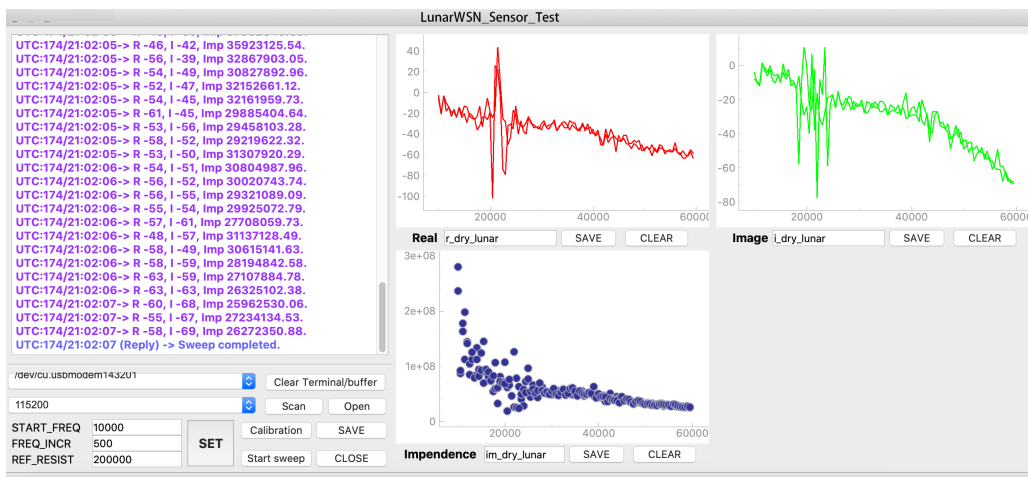
Figure 3-15: Water detection test GUI.

The impedance measurements of the sand with different water content are shown in Fig. 3-16.
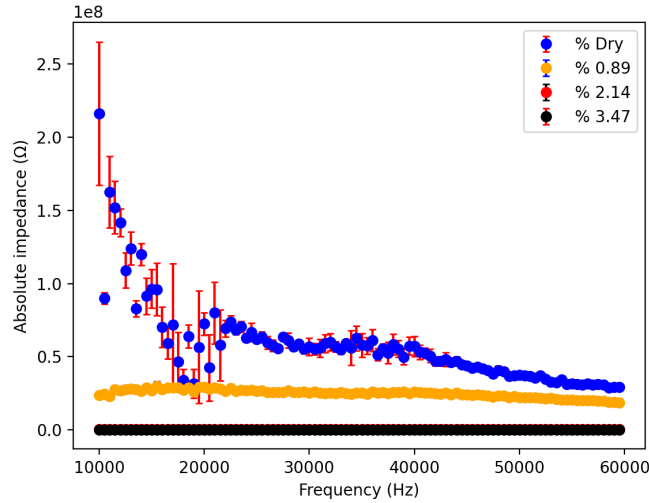
Figure 3-16: Water detection test result with sands.

Phase II — testing the sensor by using LMS-1 lunar mare soil simulant [44] with different water content (Dry, 0.87%, 1.09%, 1.42%, 2.07% by weight (wt.%)) at room temperature (24°C). The lunar soil simulant is put into a plastic cup, as shown in Fig. 3-17a. The doped ultrapure water is pipetted into the simulant. The water and simulant are mixed together by vigorous hand shaking. Every operation is finished in a glove box, as shown in Fig. 3-17b. The sensor node is put into the cup after senor calibration and the probes fully spike into the soil. The lunar simulant is very harmful to lungs, so the lid of the box is closed after the node is put inside, as shown in Fig. 3-17c.

(a)   (b)   (c)
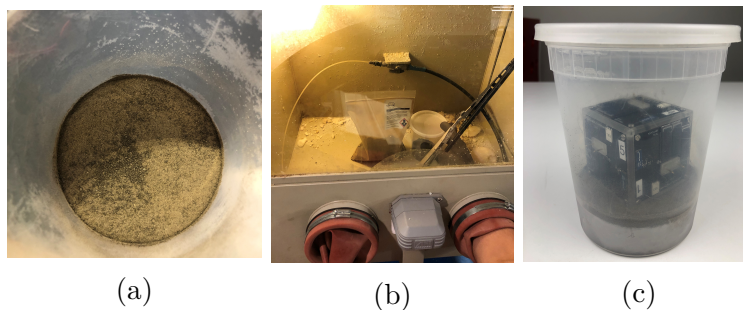
Figure 3-17: Water detection test with LMS-1.

51

The test results with LMS-1 is shown in Fig. 3-18.
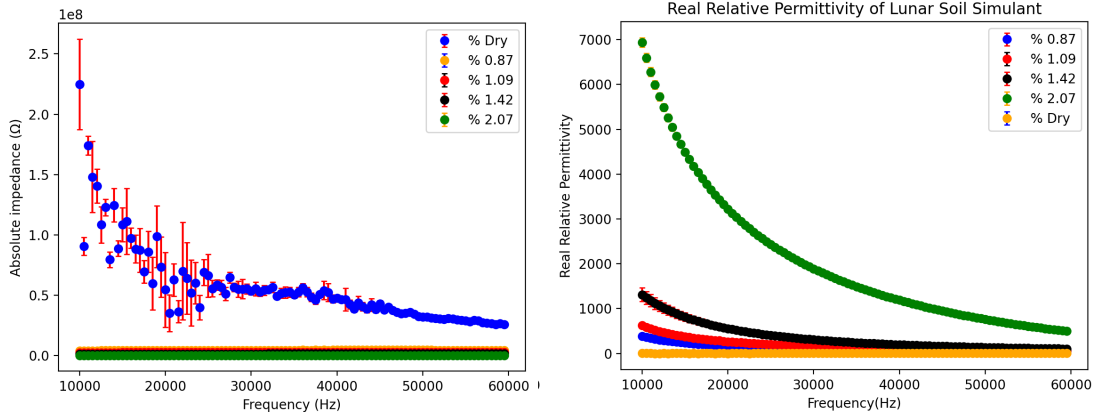
Figure 3-18: Water detection test result with LMS-1.

From the test results, we observed that the absolute impedance drops rapidly with even less than 1% of water added. The real relative permittivity increases as the water content get higher.

Chapter 4

Deployment approaches

Some deployment approaches are discussed here.

  Compressed gas projectile launcher — The PHALANX demonstrated a launcher that uses compressed carbon dioxide (CO_2) as propulsive source. The compressed CO_2 fills a chamber up to a desired pressure. The CO_2 will be released rapidly upon trigger into a barrel and a sensor node is shot out. The sensor node can be deployed up to 30 meters away under the earth gravity level [3]. The cold-gas projectile launcher is mounted on a analogue test rover, as shown in Fig. 4-1

Figure 4-1: Cold gas projectile launcher of PHALANX.

  The compressed CO_2 is a good propulsive source due to its simplicity, compactness, and ready availability [3]. However, the low temperature in some regions of

lunar surface will cause a reduced, or unstable vapor pressure of gas, which results in weakened or highly variable thrust.

Dropped by a rover — Another approach to deploying nodes in different positions is leveraging the mobility of a rover. A set of nodes can be carried by a rover, and each node can be put on the lunar surface when the rover arrives at the desired position. This approach can also guarantee that each node is in a designed orientation on the lunar surface. This is a good choice when the nodes are designed to be deployed in regions of interest that are safe for the rover's movement. But this approach can not show the advantage of the WSN technique in exploring hard-to-reach areas and will use precious rover's operating time.

Spring gun — A projectile launcher with elastic components, such as springs, is another approach to impart momentum to the sensor nodes. By repeatedly tensioning the spring and shooting the node out, multiple nodes can be deployed. The surface of the moon is a vacuum and the movement of the nodes will not be affected by air. Therefore, their rough dropping points would be easily predicted. However, a repeat tensioning mechanism necessitates more power consumption. The springs are also temperature sensitive. Such a projectile launcher has multiple moving parts, which are risky due to the strong vibrations during the launching phase.

Another idea is using a structure like a gun magazine, as shown in Fig. 4-2.
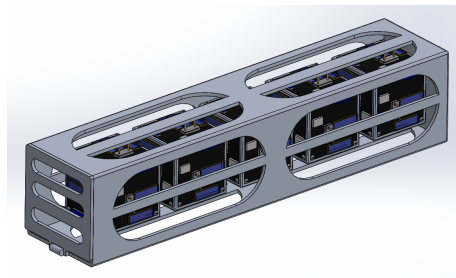
Figure 4-2: Sensor node magazine.

The magazine is loaded with sensor nodes to be deployed. A spring is installed on the inside of the bottom of the magazine and pushes the nodes out one-after-another. The magazine is installed inside a rover, and the sensor nodes can be deployed to regions of interest, as shown in Fig. 4-3.

Figure 4-3: LunarWSN nodes deployed from a rover.

This approach avoids repeatedly tensioning the spring. After some nodes are shot out, the spring gets longer, and if the spring is non-linear, the stiffness is not constant. So the force applied to each node will be different. This will cause non-identical deployment distances. But this kind of error can be estimated. This kind of launcher is simple, low-cost, and robust. For miniature sensor node deployment, this is a very feasible approach. The inside of the magazine needs a careful design, since the surface of the node is not flat due to the protruding sensor probes and other components, hence the magazine needs to avoid sensor nodes being jammed.

Chapter 5

Conclusions, Limitations, and Future work

5.1 Conclusion

We presented the LunarWSN concept to expand WSNs to space applications. We aim to explore one of the most valuable resources for future lunar missions — water. We showed a miniature (5cm×5cm×5cm) and modular LunarWSN sensor node design and tested its performance in a lab environment. The node uses a off-the-shelf 2.4GHz radio for wireless communication, and the range for a robust wireless communication connection is 7.5~8m. The wireless positioning tests demonstrated a maximum 0.49m error on the X-axis and a maximum 0.69m error on the Y-axis. The water detection sensor measures the permittivity of the lunar soil simulant with different water content. The results show that the sensor measurements can detect the differences of lunar soil simulant permittivity and infer the different water content. Our work shows promise for the LunarWSN node to be used in future lunar applications.

5.2 Limitations and possible solutions

While we demonstrated basic functions of the sensor node, several imprvements need to be made (e.g., RF/localization range) before a deployment would be feasible. Other sensor approaches and modifications are also discussed below.

5.2.1 Positioning

Localization capability is one of the most fundamental features often offered by a WSN [45]. The nodes' positions are crucial for not only mapping and visualizing science data, but also helping with the localization of other movable systems, such as planetary rovers [46]. As reported before, the current positioning function is realized by leveraging wireless ranging and triangulation. However, during the development and test of this function, some limitations were found.

Power consumption

The current UWB radio used for wireless ranging is very power-consuming ($\sim 1W (\sim 250mA@4.2V)$). Although the wireless ranging is performed only once, since the node does not have mobility and the position will not change after deployment, the power consumed is still sufficiently large enough to not be ignored. Moreover, in real working cases, the time over which the wireless ranging lasts is uncertain, since the node will try to find all ranging anchors and adjacent nodes within the RF range to get the best positioning performance [47]. This will lead to higher power consumption.

RF design complexity

During the positioning test, sometimes a node would not find all ranging anchors after it was put on the floor with a random orientation, but all anchors could be found with a small adjustment to the node's orientation. This shows a strong directionality of the node's antenna design, and that the antenna radiation pattern can not cover all directions. The antenna design is very tricky, and it's not that easy to keep good RF quality, especially with such a high frequency (4GHz $\pm$ 250MHz). The current design

uses chip antennas, whose performance is easily impacted by adjacent components with metal, such as solar panels, screws, and internal PCBs that are on the back of the antennas. To get a better understanding of the RF performance of the node design, high-grade simulation and analysis are essential.

Possible solutions

Some other approaches for positioning can be adopted.

- *Leveraging Received Signal Strength Indication (RSSI)*

The current design uses two sets of radios for wireless communication and wireless ranging. This increases the complexity of the design. A better solution is using only one radio to realize both. The current UWB radio for wireless ranging can also transmit messages, but the power consumption is unacceptable. Another solution that is widely used for WSN localization is RSSI. By leveraging a statistical model of radio propagation and received signal strength measured from the reference anchors, the distance between the anchor and the node can be estimated. RSSI is supported by many low-power wireless communication ICs and widely used in indoor localization. However, the complex indoor environment changes over time and has strong multipath effects. This introduces very large errors to localization. On the lunar surface, the environment is relatively static. With a proper RF propagation model, the multipath effect can be reduced. Using spread-spectrum methods is another approach to diminish the multipath effect. This benefits the RSSI implementation and could enable high-accuracy localization. The shadowing effect, which is caused by signal attenuation due to obstructions, is another challenge [48]. RF propagation models to analyze the multipath and shadowing effects on the lunar surface are presented by many research [48–51]; if a node lands behind a mountain, shadowing effects could be significant.

- *Lunar GPS*

Upon the return of people to the moon, a Lunar GPS would be essential, for not only autonomous systems but also astronauts' safety [52].

Like the Global Navigation Satellite System (GNSS) used on the earth, it's also

promising to build a GNSS system for Lunar space. There are mainly two approaches to implement this goal. The first approach uses the current navigation satellites on earth orbit; although most of the energy of their navigation antennas radiates directly towards the Earth, the signals from the antennas' side lobes can be employed for positioning of satellites in lunar orbit, provided a high sensitivity receiver [53] or high-gain navigation satellite antenna [54] is implemented. Another approach is building a lunar orbital constellation for Positioning, Navigation, and Timing (PNT) by using a CubeSat system and the Chip-Scale Atomic Clock (CSAC) [55].

The nodes in the LunarWSN can take advantage of such future GNSS infrastructure to localize themselves. However, this would need many prior missions to set up the Lunar GPS system, and both approaches put forward requirements for the radio system to receive signals from the GNSS constellation.

- *Mobile ranging anchor*

One of the most promising deployment approaches for the LunarWSN is being deployed from a rover, as shown in Fig. 4-3. The current idea for positioning is having the rover install all the ranging anchors, and after a node was deployed, the position of the node can be calculated by leveraging wireless ranging and triangulation, as mentioned in Section 3.1. The placement and density of anchors are crucial for wireless positioning performance, and the location estimates of the nodes are usually more accurate with a higher density of anchors [56, 57] However, the space on the rover is limited, which means only limiting anchors can be installed, and the anchors will be very close to each other. In the meantime, multiple anchors will increase the cost of the system and the complexity of the rover.

Instead of installing multiple anchors on a rover, we can take advantage of the mobility of the rover and install only one anchor on it. After the rover reaches a new position, it can serve as a new anchor, as shown in Fig. 5-1. The rover at N different positions $((x_1, y_1), (x_2, y_2), ..., (x_N, y_N))$ of its path serves as N anchors and gets the relative distance of the node on each position $(d_1, d_2, ..., d_N)$. Then the position of the node $((x, y))$ can be calculated by using the approach described in section 3.1.

This approach simplifies the system design and requires much fewer modifications
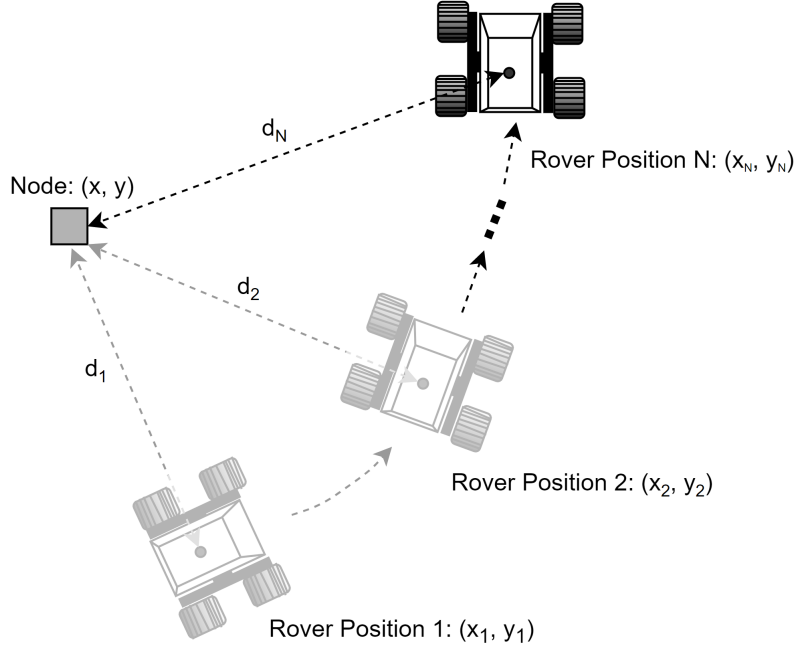
Figure 5-1: Positioning with mobile anchor.

on the rover. The performance of this method will highly depend on the localization accuracy of the rover. The rover can employ dead reckoning for localizing itself, and as the rover has much higher power capacity and a bigger internal space, it can also use more accurate positioning approaches that have higher requirements on hardware and power, such as image processing [58, 59], star tracking [60], and the GPS mentioned above. However, this approach needs to repeatedly trigger the nodes for wireless ranging at different rover positions, especially when higher accuracy is expected, more measurements from more positions are essential. This will make the wireless ranging process longer and increase power consumption.

The rover's positions are not indispensable for the localization of sensor nodes in such a distributed sensor network. In [61], a Pinger device generated ultrasound emission at random locations, and the nodes measured the time-of-flight, hence derived their distances from the Pinger. By leveraging the distance measurements of each node and the described localization algorithm, the system was able to localize each sensor node with centimeter accuracy. This technique can be used for the localization of LunarWSN nodes (using RF timing instead of ultrasound). The rover serves as the "pinger" here and triggers the nodes' wireless ranging at different locations. The

location of each node can then be attained without needing to know the positions of the rover.

5.2.2   Energy harvesting

Solar energy harvesting is probably the most widely-used energy harvesting approach for all space systems [62]. However, for systems operating on the lunar surface, lunar dust will significantly impact the performance of the solar panels [63]. The lunar dust is extremely adhesive and difficult to get rid of [64]. The LunarWSN node will be rolling on the lunar surface after touching down. This will let the node get significant dust adhered to the surface and significantly reduce the solar panels' performance.

Possible solutions

Some other energy harvesting approaches are considered.

- *Radioisotope Heater Unit (RHU)*

The RHU is small devices (shown in Fig. 5-2) that uses the decay of plutonium-238 to provide heat.

Figure 5-2: Radioisotope Heater Unit.

An RHU contains a Pu-238 fuel pellet about the size of a pencil eraser and outputs about 1 Watt of heat continuously for decades [65]. This heat can be used for keeping the internal temperature within a proper range for the components/battery operations

during the lunar night and generating power with the help of thermoelectric generators [66–68].

Pu-238 emits primarily alpha particles [69], and Alpha particles can be easily shielded by simple barriers such as a thin sheet of paper [70]. High heat density and low shielding requirement make the RHU a light unit and can fit in small cubic space. However, the greatest limitation of Pu-238, a manufactured isotope, is the difficulty of making it in sufficient quantities [69]. As we want to deploy tens and even hundreds of LunarWSN nodes on the Lunar surface, it will not be very feasible to equip each node with an RHU.

- *Temperature differences within the node*

The surface of the moon is a vacuum, and the temperatures depend largely on whether a point is in sunlight or in shadow [71]. The node sides in sunlight would be much hotter than the ones in the shadow. With the help of a thermoelectric generator, this temperature difference would be a very promising source for energy harvesting.

5.2.3   Wireless communication capability

Wireless communication is the most fundamental capability for the node to set up a network for relaying data and commands. The current design is using a off-the-shelf 2.4GHz radio for communication. As reported before, the communication range is very limiting and easily impacted by obstructions.

The number of the nodes in a WSN is up to the communication capability and requirement of data density. The communication range needs to be large enough to cover the regions of interest.

For a multi-hop WSN, n is the number of nodes that are randomly deployed in a round area with a unit radius. For such a WSN, if all sensor nodes have the same communication range, then the communication range r to keep a robust network within the WSN is given by [72]

$$r(n) \geq R\sqrt{\frac{2logn}{n}} \tag{5.1}$$

Where R is the radius (in m) of the round area. The LunarWSN node is about 150g. Then 1kg of payload can carry about six sensor nodes. According to our test, the communication range of each node is ∼7.5m. Then according to equation 5.1, the maximum radius of a round area in which six LunarWSN nodes can cover is ∼14.7m, which is not very big. Although the communication range is determined by mission requirements, we still hope to get a 100m range, which offers enough margins for different missions.

One solution is adopting a radio that supports transmissions over long distances with low power consumption, normally lower frequency radio, such as the LoRa (Long Range). The radio diffraction is noticable when the wavelength is comparable or larger than the size of obstacles. Therefore, lower frequency radios can help reach the nodes behind mountains.

A simple cubic node equipped with a LoRa radio is made to prove the performance of this radio. This node is very small ($42mm \times 42mm \times 42mm$). The node uses LoRa radio at 915 MHz, giving a quarter-wave monopole antenna size of 8.2 cm. This is very large compared with the size of the node. So we installed the monopole antenna in the frame of the node, as shown in Fig. 5-3.

Figure 5-3: A sensor node with LoRa radio.

We tested the communication range of this design in an outdoor environment and observed that the communication range can reach more than ∼30m, which can

increase the radius of the area to $\sim$58.9m. The LoRa radio, however, can reach more than 10km [73]. The electronics and metal components behind and around the antenna could significantly impact the antenna performance. Therefore, more high-grade RF design of the node is needed. The power consumption of the LoRa radio (TX: 20mA@+7dBm; RX: 9.9mA) [74] is also comparable with the current 2.4GHz radio (TX: 11.3mA@0dBm; RX: 13.5mA) [32]. A drawback comes with the long distance connectivity is a lower data rate. The 2.4GHz radio can offer a data rate up to 2 Mbps, but LoRa radio data rate is 300 kbps at best. We don't anticipate frequent or bully data transmissions in the network, so 300 kbps should be adequate. We can also improve the communication performance by using a high gain omnidirectional antenna for the central station to increase its transmission power.

As the node will be deployed on the lunar surface, the radio performance will also be impacted by the surface terrain. Another approach to improve the communication capability is to enable the antenna to stand off the surface and provide a line of sight over the obstacles on the surface. This can be realized through a self-righting design, which is discussed in Section 5.2.4.

5.2.4 Too much redundancy

The current cube-shaped node design has antennas, solar panels, and sensor probes on every side. This guarantees an omnidirectional RF connection and sensor contact with the lunar surface, hence can improve the robustness of the design. However, this design will cause much waste and significantly increases the node complexity and cost, along with added workload in design, manufacturing, and test phases.

Some new kinds of node designs that can guarantee an omnidirectional RF connection and less redundancy at the same time are discussed.

One option is to equip the node with mobility to self-right itself to the desired orientation after landing. This makes the antenna always standing right up and above obstacles to providing a line-of-sight for RF connectivity. In this case, only one antenna for each set of radio is needed. This will significantly simplify the design.

Three promising designs to realize this goal are described below.

The first approach is using a "mobility" system that is similar to the Mobile Asteroid Surface Scout (MASCOT) [75] onboard the Hayabusa2 mission [79], as shown in Fig. 5-4.
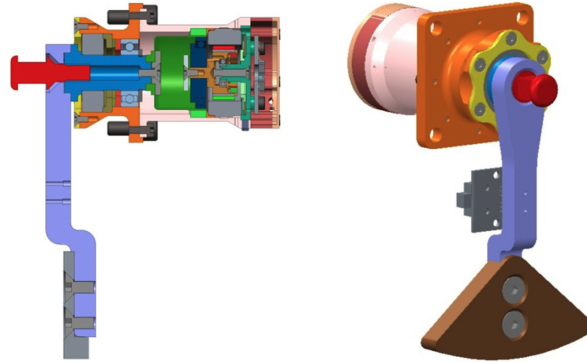
Figure 5-4: CAD sectional drawing of the MASCOT's mobility unit.

After the MASCOT free-falls onto the asteroid surface, with the help of the "mobility" system, it can self-right itself to the normal orientation, so that the onboard IR imaging spectrometer, camera, and radiometer can properly operate.

The mobility system uses a small brushless DC motor with only 25mm diameter to accelerate and decelerate an eccentric arm. The resulting reactive force applies torque to MASCOT, which enables the MASCOT to hop or to self-right to its nominal position with the help of the low gravity level on the asteroid surface [75]. A similar system can be used in a small sensor node, since such a mobility system is so compact.

Another design is including flywheels housed within a sensor node. The flywheels can spin and abruptly brake to bring the cube varying amount of torque. This enables the cube to hop or just roll to adjust the orientation after landing. This kind of mobility system has been used and approved valid in the cube-like rover — "Hedgehog" (shown in Fig 5-5.) [76]. The "Hedgehog" is designed for exploration of asteroids, comets.

Another system that uses flywheels as the mobility strategy is the "M-Block" [77, 78] developed by MIT CSAIL, as shown in Fig. 5-6.

There is one flywheel inside each M-Block, and by leveraging the angular momentum when the flywheel is braked, the M-Block can jump, spin, and flip.
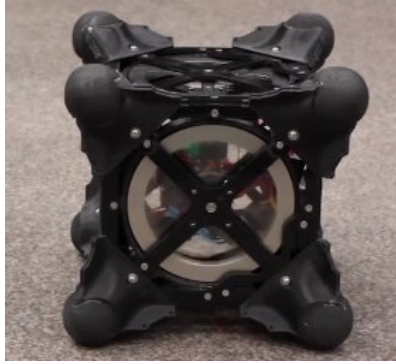
(a) The Hedgehog cubic rover.
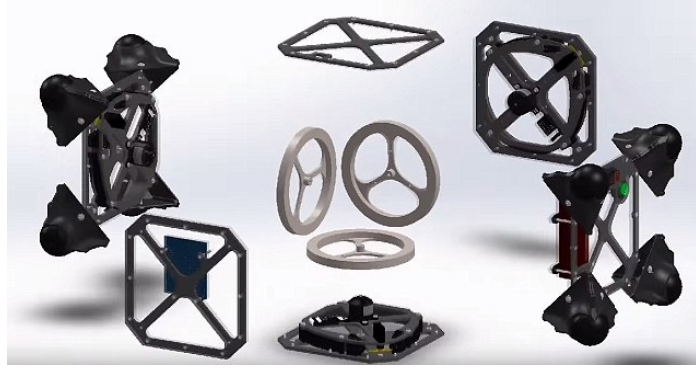
(b) The exploded view of Hedgehog.

Figure 5-5: Hedgehog: a cubic rover that may one day explore some of the most extreme environment in solar system.

Figure 5-6: One modular robotic cube snaps into place with rest of the M-blocks.

Both designs can not only enable the node to self-right to normal orientation, but also give the sensor node mobility. Many different mobility concepts have been studied, including legged robot [80,81], climbers [82], hoppers [83], helicopter [84], and snakes [85]. This mobility is essential for providing much denser data from an area by using a limited amount of sensor nodes. However, all these designs use actuators (such as motors) to get mobility, and these actuators are very power-consuming, especially when the nodes need to go across a long distance. This brings pressure to the power budget. Systems, such as hoppers, helicopters, snakes, etc., all need a sophisticated mechanical system and moving parts, which are risky due to the strong vibrations during launch.

Another design is shown in Fig. 5-7a. This design includes support arms that can expand to support the node to stand-up. Each support arm is driven by a spring hinge and locked before deployment. After the node lands on the surface, the locked

support arms will be released and expand. The node will self-right and start working, as shown in Fig. 5-7b.
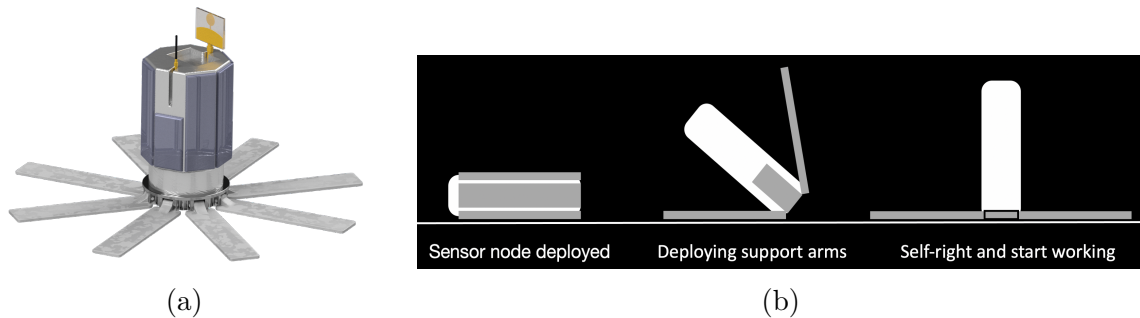
Figure 5-7: (a) CAD drawing of a automatic standup sensor node design. (b) The node's self-right motion.

This design uses non-power-consuming actuators — springs, which avoids extra power consumption. However, this design doesn't have any mobility to enable the node to move around. Therefore, this design is better for the missions in which the nodes need to perform long-term monitoring of environmental data (such as the variation of radiation dose over time) from fixed positions.

Another approach is making the sensor node passive self-righting, like a tilting toy. However, the self-righting may not function well with thick dust on the lunar surface.

5.3   Other possible sensor payloads

There are some limitations of current sensor: (1) As the sensor probes are so short, they can only protrude into the lunar dust and regolith for a centimeter to a couple of millimeters, hence the node can only detect the surface water content. (2) The proper operation of the sensor is based on the assumption that the sensor probes will fully protrude into the lunar soil, or else the measurement will be inaccurate. If the node lands in thick dust, it may settle on a corner, without any probes protruding into the lunar surface. (3) The water content in the lunar regolith will not change rapidly over time, which means the data collected by the node will be the same over a long time.

(4) The water exists in PSRs, and the softness of the soil there is unknown. Maybe the soil is very rigid and the probes can no protrude into it.

The LunarWSN is a versatile platform and can perform many other sensing missions. Some are discussed here.

5.3.1 GPR (Ground Penetrating Radar)

The current sensor node has a UWB antenna on each side for wireless ranging. After the node has landed on the surface, it will traverse all UWB antennas to find the one that can provide the best RF connectivity. After this process, all the other antennas, especially the one on the bottom, are spare and may not be used for wireless ranging anymore.

The Chinese Yutu-2 rover has a onboard dual-frequency Lunar Penetrating Radar (LPR) and unveiled the lunar farside shallow subsurface structure [101]. The Lunar-WSN sensor node can take advantage of the spare antenna on the bottom and compose a Ground Penetrating Radar (GPR). An impulse GPR can delineate subsurface interfaces between materials with different dielectric and/or structural properties [86]. The UWB antenna on the bottom can serve as the GPR antenna. It is in contact with the regolith and can provide the strongest signal strength.

The penetrating depth depends on the complex dielectric constant of the lunar soil, GPR frequency, and the GPR transmission power. A recent estimation of the dielectric constant of the lunar regolith is 2.5 to 3.4, and the penetration depth varies from 3 to 10 wavelengths over Maria, and from 20 to 25 wavelengths over highlands [86]. The operating frequency of the UWB antenna is $3.1\text{GHz} \sim 5\text{GHz}$, which gives the best penetration depth of $\sim 2.5\text{m}$. However, a higher GPR frequency can provide an improved depth resolution [88].

A GPR can also be used for detecting the existence of water ice buried under the lunar soil. However, it can be effective only when the ice is in a thick deposit $(\sim 10\lambda)$ of nearly pure water, since small grains of ice mixed into the regolith will not cause a big change in the dielectric constant of the lunar soil [89].

To implement a GPR, the node needs a new set of radio composes. For now,

there are some chip-scale COTS pulse radar modules, such as A111 [90], XR112 [91], etc. Most of the pulse radar modules have Antennas in Package (AiP). Using these modules can not take advantage of the spare UWB antennas. Therefore, we would prefer a custom-designed GPR, such as a Frequency Modulation Continuous Wave (FMCW) radar.
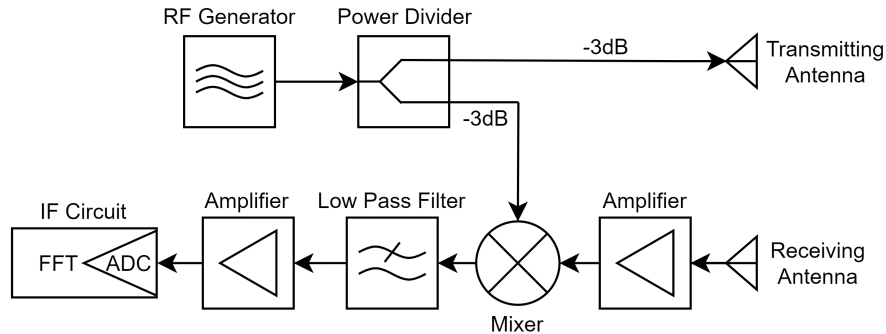
Figure 5-8: Block diagram of a simple FMCW radar system.

As shown in Fig. 5-8, an FMCW radar needs an RF front-end and an Intermediate Frequency (IF) circuit for processing Fast Fourier Transform (FFT). A big limitation of this sensor is power consumption. For getting good transmission and penetration performance, a GPR needs high transmission power. For example, the IWR1843 Single-Chip FMCW transceiver [92] consumes more than 1W for normal operation. This will be a burden for a small sensor node with a limited power capacity.

5.3.2   Environmental sensing

The LunarWSN can be used for monitoring environmental conditions of the regions of interest, such as lava tubes, which hold promising potential for serving as future sustainable lunar habitats. Some sensor payloads for such missions are discussed below.

Radiation monitoring

Long exposure to radiation on the lunar surface holds a substantial risk to astronauts in human exploration missions on the moon. On the lunar surface, this radiation

consists of chronic exposure to Galactic Cosmic Rays (GCR) and sporadic solar particle events [93]. A comprehensive understanding of this radiation is essential for the development of radiation tolerant, hardened systems, and radiation protection equipment.

China's Chang'E 4 lander has made the first-ever measurements of the radiation for both charged and neutral particles on the lunar surface [93]. However, without mobility, the lander measured the radiation from only one point on the moon. To get a comprehensive understanding of the radiation condition on the lunar surface, measurements from multiple points over time are essential. This would be a scenario that the LunarWSN fits. LunarWSN nodes can perform simultaneous observations of the radiation variation over time from different positions.

A promising COTS sensor is Timepix, which is developed by the CERN (European Organization for Nuclear Research) for particle physics related applications. The Timepix chip is a silicon-based hybrid pixel detector that is in a size of 1.4cm × 1.4cm and contains 256 × 256 pixels [95]. At CERN, the latest version of Timepix, Timepix3 [96], as shown in Fig. 5-9a, has been used for particle detection and tracking in the LHCb [97, 98] and ATLAS [99].
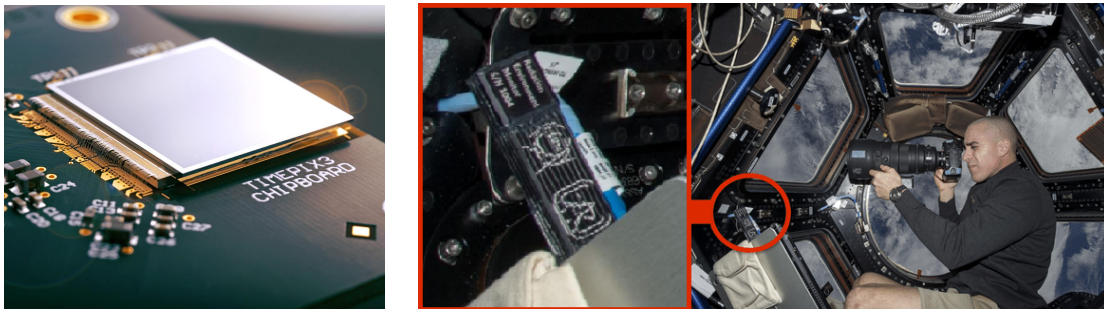
(a) The Timepix3 chip. (b) Timepix equipped USB device on the ISS.

Figure 5-9

The Timepix is also used for measuring radiation dose on the International Space Station (ISS) [100], as shown in Fig. 5-9b, and help better understand the radiation spectrum in the ISS and how to protect the crews.

Multiple Timepix chips can form a particle telescope. Each LunarWSN node equipped with a Timepix telescope and a read-out circuit can perform 3D charged

particle tracking [101,102] and neutron detection [103]. The sensor may have requirements on the node orientation since an unobstructed Field Of View (FOV) is better for radiation measurements. The node does not need to be perfectly vertical to the Lunar surface since the GCR radiation field is isotropic [93].

The problems of using pixel particle sensors are the price and power-consumption (1-2W). We can use silicon photodiodes instead to make particle sensors as described in [94].

Seismology

The "Moonquake" is first discovered by Apollo mission, and four types of moonquakes are found: (1) Deep Moonquake; (2) Thermal Moonquake; (3) Shallow Moonquake; (4) Meteoroid Impacts; (5) Moonquake. Passive seismometers were installed on the lunar surface during Apollo missions 11, 12, 14, 15 and 16 [104], and the information collected by these seismometers yield information regarding seismicity, structure, and the lunar regolith. However, the Apollo seismic stations only covered the front center of the Moon in an approximate equilateral triangle with 1,100km spacing between stations [105]. This limited span of the Apollo seismic network left a lot of unknowns. For example, the structural and thickness variation of the Lunar crust, the existence and character of the magma ocean, The nature of the deep lunar interior, The composition of the moon's core, etc [106]. All these questions pose a scientific need for a new broadly spanning seismic network. The new seismic network needs to perform a longer operation (5∼7 years [106]) to collect more data with high quality for a better understanding of the origin and evolution of the Moon [107]. These data are also essential for the future sustainable human presence on the moon. As Shallow Moonquakes and Meteoroid impacts are hazardous for a future long-term lunar outpost (5.5 moonquakes on the Richter scale have been recorded by the Apollo seismic experiment) [106]. The data collected by the new seismic network is also essential for (1) Building a statistic analysis of meteorite impacts for determining if the potential positions for the future Lunar outpost have low probabilities of receiving hazard meteorite impacts. (2) Understanding the nature and location of the shallow moon-

quakes, and making sure the potential positions for the future Lunar outpost are not seismically active [106].

The LunarWSN can help with building broader seismic networks in regions of interest on the lunar surface. The lightweight and small-size node guarantees a network with more sensors to provide higher-quality seismic data, since the arrays of sensors may tremendously improve the dynamic range by reducing ambient and coherent noise [108]. A normal sensor for seismic event sensing is a coil-based geophone (as shown in Fig. 2-6a). These Geophones are a proven rugged, cheap, and self-powered sensor. To measure ground movements on all directions, multiple geophones are required. Geophones are big (a cartridge with a length of ∼3 cm). Multiple geophones may not be able to fit in a small node. Geophones are also heavy (∼75g). Multiple geophones in a single node will make a whole set of sensor nodes very heavy.

(a) SM-24 Geophone   (b) ADXL355 accelerometer.
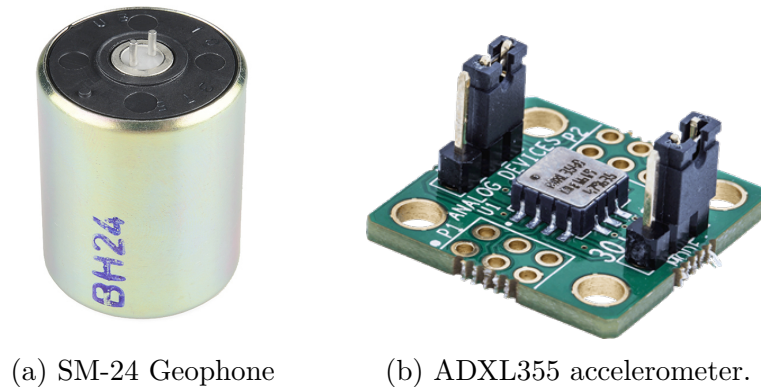
Figure 5-10

Therefore, smaller, and light-weight seismic sensors are essential for building a large-scale seismic network. This trend suggests the utility of Micro Electro Mechanical System (MEMS) accelerometers, such as the ADXL355 [109] (as shown in Fig. 5-10b), a three-axis accelerometer that is capable of seismic imaging. MEMS accelerometers are very small (with a length of less than 1 cm) and light (less than 1g). Most current MEMS accelerometers can measure the movement of the ground in 3 axes. Compared with geophones, the benefit of MEMS accelerometers is a broadband linear amplitude and phase response that may extend from 0 to over 1kHz [108], and this guarantees a wider frequency response compared with the geophones used in

the Apollo missions, which are sensitive from 0.05 Hz to 10 Hz [110]. Moreover, this broadband response makes it possible to use MEMS accelerometers to record low frequencies (for the Moon, we intend to focus on a frequency band of $0 \sim 40$ Hz) without attenuation [110]. However, compared with geophones, MEMS accelerometers have higher self-noise, which is the most limiting parameter for resolution [111].

A moonquake is longer than an earthquake [112], and last for up to an hour [113]. The communication connectivity within the WSN will not be constantly available. A built-in memory for temporality data storage is necessary, and the memory should be big enough to store the data of a long seismic event. Power consumption is also another concern since it will take longer time for a node to send out the all seismic event data. Another challenge needs to be solved is that the free-falling sensor nodes need to have good coupling with the lunar surface.

5.4   Future work

Future work needs to be done to complete the system and improve the performance.

- Integrating all the subsystem programs into a complete version of node firmware, and test the node functions, performance, and robustness for at least two weeks of operation, which is as long as lunar daylight.

- RF pattern measurements. During the wireless positioning test, we found that sometimes the node can not find all ranging anchors in some orientations. The terrain interference and indoor multi-path effect might be the reasons. The strong Radiation directionality would be another reason. The radiation pattern of the node may not be able to cover the whole space. The radiation pattern measurement of this node design needs to be done in an RF anechoic chamber. This is to guarantee robust RF connectivity.

- Water detection test at low temperatures. The lunar water is found in polar regions PSRs [114], where it is extremely cold (as low as -233°C [115]). With the same water content, the permittivity of lunar soil behaviors differently at such a low temperature than at a room temperature [116]. More sensor tests at low temperatures

are essential to guarantee a robust sensor performance in a relevant environment.

- The current work only focused on the development of a single node. For future work, a network composed of dozens of nodes will be built.

- Exploring different sensor payloads. For example, for seismic sensing, besides MEMS accelerometers, an optical accelerometer [117] is a very promising candidate. Compared with the ADXL355 shown in Fig. 5-10b, the COTS optical seismometer from Silicon Audio [117], as shown in Fig. 5-11a, has low noise ($20ng/\sqrt{Hz}$, by contrast, the ADXL355's noise is $22.5\mu g/\sqrt{Hz}$ [109]) and a broadband (0.1-1kHz) [111]. It's a seismic instrument that is competitive with state of the art planetary seismometers [118]. Another very promising candidate is the Molecular electronic transducers (MET) seismometer [119], as shown in Fig. 5-11b. The MET seismometer also has low noise (as low as $10ng/\sqrt{Hz}$) and a broadband (1-300Hz). However, a MET seismic sensor would be very heavy (7.5kg) and its bandwidth would be very limited (0.0167–50 Hz) [119] if low noise level is required.

(a) Optical seismometer from Silicon Audio.
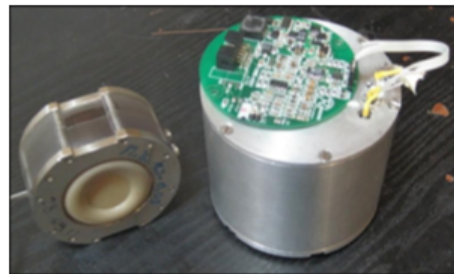
(b) Assembled MET sensing cell, sensor circuits and protection cell

Figure 5-11: (a) Energy harvesting test setup (b) experiment diagram

- Exploring more energy harvesting approaches. The solar irradiance condition used in energy harvesting test is the average condition. The effective solar irradiance at the South and North Poles are $37.3W \cdot m^{-2}$ and $38.0W \cdot m^{-2}$, respectively [41], which are much lower than the average level. In this irradiance condition, the energy harvested may not be enough. This necessitates a new node design with bigger solar panel areas, or solar panels with higher power output, or a new energy harvesting approach. The solutions to the energy harvesting problems mentioned in section

5.2.2 use thermoelectric generators. However, thermoelectric materials have very low efficiency [120]. A lightweight tower structure [121] can be used for powering the sensor nodes. With the top of the boom installed a laser power beaming equipment, the tower can provide power for sensor nodes surrounding it. It is mentioned in [93] that on the lunar surface, without the protection of the atmosphere, the radiation from galactic cosmic rays and sporadic solar particle events is very strong. This could be an inexhaustible resource for energy harvesting. Some research has been conducted on harvesting energy from this kind of radiation [122, 123], and this new technology could benefit the exploration of the moon, especially the explorations in PSRs or during the lunar night.

Appendix A

Schematic of each module

U2
SKY13416-485LF

RF1 RF2 RF3 RF4 RF5 RF6
BIAS
Decoder
VBB V1 V2 V3
PAD
GND
J8

rang_V1 7
rang_V2 6
rang_V3 5

J14
J12
J10
J6
J4
J2
GND

FB2
+3.3_2
C1 10uF
C2 10nF
GND

J16
1 +3.3_2
2 rang_V1
3 rang_V2
4 rang_V3
5 X
6 X
7 GND

U1
SKY13416-485LF

RF1 RF2 RF3 RF4 RF5 RF6
BIAS
Decoder
VBB V1 V2 V3
PAD
GND
J7

com_V1 7
com_V2 6
com_V3 5

J13
J11
J9
J5
J3
J1
GND

FB1
+3.3_1
C3 10uF
C4 10nF
GND

J15
1 +3.3_1
2 com_V3
3 com_V2
4 com_V1
5 X
6 GND

H1 H2 H3 H4
GND GND GND GND

U2 NRF52832-QFAA-R

VDD VDD VDD DEC4 DEC3 DEC2 DEC1 DCC NC
P0.00/XL1 P0.01/XL2 P0.02/AIN0 P0.03/AIN1 P0.04/AIN2 P0.05/AIN3 P0.06 P0.07 P0.08
NFC1/P0.09 NFC2/P0.10 P0.11 P0.12 P0.13 P0.14/TRACEDATA_3 P0.15/TRACEDATA_2 P0.16/TRACEDATA_1 P0.17 P0.18/TRACEDATA_0/SWO P0.19 P0.20 P0.21/nRESET P0.22 P0.23 P0.24 P0.25 P0.26 P0.27 P0.28/AIN4 P0.29/AIN5 P0.30/AIN6 P0.31/AIN7
SWDCLK SWDIO ANT XC1 XC2
VSS VSS VSS/PAD

GPIO_7 GPIO_8 GPIO_9 GPIO_10 GPIO_11 GPIO_12 GPIO_13 GPIO_14 GPIO_15 GPIO_20 nRESET SWDCLK SWDIO GPIO_16 GPIO_17 GPIO_18 GPIO_19 IRQ SPICLK SPIMISO SPIMOSI DWM_RSTn SPICSn

nRF24_IRQ nRF24_MISO nRF24_MOSI nRF24_SCK nRF24_CSN nRF24_CE

Y1 32.768kHz
C26 12pF C30 12pF

C27 4.7uF C28 1uF C29 0.1uF DEC4
L1 10uH L2 15nH DEC4
C15 100nF C16 NC C17 100pF C18 1uF
R25 R26

U4 AP2112K-3.3
VIN VOUT EN GND
C42 10uF C43 10uF C44 0.1uF VCC

U5 TPS62202DBV
VI SW EN FB GND
L6 10uH C41 10uF C40 4.7uF C50 0.1uF R6
+1V8 +3.3V EXTON

J3
GPIO_16 GPIO_17 GPIO_18
R19 78.7K R20 78.7K R21 78.7K
SWDIO SWDCLK
R16 100K R17 100K R18 100K
+3.3V

GPIO_8 GPIO_9 GPIO_10
R13 78.7K R14 78.7K R15 78.7K
R7 100K R11 100K R12 100K
J8

U1 DW1000-I-TR13

SPIMISO EXTON
VDDLDOA VDDLDOD VDDIO VDDIO VDDIOA VDDAON VDDPA2 VDDPA1 VDDLNA VDDBAT VDDDIG VDDREG VDDVCO VDDSYN VDDCLK VDDIF VDDMS XTAL2 EXTCLK/XTAL1 VREF CLKTUNE VCOTUNE RF_P RF_N FORCEON WAKEUP SPICSn RSTn
NC NC NC NC
GND GND VSSIO VSSIO
SYNC/GPIO7 GPIO6/EXTRXE/SPIPHA GPIO5/EXTTXE/SPIPOL GPIO4/EXTPA GPIO3/TXLED GPIO2/RXLED GPIO1/SFDLED GPIO0/RXOKLED SPIMOSI SPICLK IRQ/GPIO8 TESTMODE

R1 11K R2 0 R3 0
CLKTUNE VCOTUNE
SPICSn DWM_RSTn
RF_P RF_N
SPIMOSI SPICLK IRQ

VDDLNA FB3 C24 0.1uF +3.3V
VDDPA2 FB2 C11 330pF C10 10pF C9 0.1uF +3.3V
VDDPA1 FB1 C8 330pF C7 10pF C6 0.1uF +3.3V

VDDIOA C49 0.1uF +3.3V
VDDLDOA C14 4.7uF +1V8
VDDAON C25 0.1uF +3.3V
VDDLDOD C13 0.1uF +1V8
VDDBAT C12 0.1uF +1V8
VDDSYN C23 4.7uF +3.3V
VDDIO C22 0.1uF
VDDMS C21 0.1uF
VDDIF C4 0.1uF
VDDDIG C3 0.1uF
C1 0.1uF C2 0.1uF

Y2 CX2016DB38400F0FSRC1
L3 C31 12pF
C20 1.2pF VDDCLK CLKTUNE
R8 16K C46 27pF C5 0.1uF

VCOTUNE C45 18pF
VDDVCO R9 270 C47 820pF C48 0.1uF

BALUN1 HHM1595A1
GND NC UN BA_1 BA_2
C33 12pF C34 12pF +3.3V

J2 U.FL-R-SMT_10_

U3 NRF24L01P-R7
ANT2 ANT1 VDD_PA VDD VDD VSS VSS VSS VSS EP CE CSN SCK MOSI MISO IRQ XC2 XC1 DVDD IREF VSS

ANT1 2450BM14A0002T
BAL_1 BAL_2 GND DC/GND UNBAL NC
C52 2.2nF

C37 1nF C38 10nF C39 1uF
X1 NX2520SA-16MHZ-STD-CSW-5
R4 1M C56 6pF C55 6pF
R10 22K C54 33nF

J9 R22 100K R23 100K R24 100K

nRF24_CE R27 nRF24_CSN R28 nRF24_SCK R29 nRF24_MOSI R30 nRF24_MISO nRF24_IRQ

J1
VCC GPIO_12 GPIO_13 GPIO_14 GPIO_15 GPIO_11 GPIO_20 GPIO_7 nRESET

Y3 R2016-32.000-8-F-1010-EXT-TR
C35 12pF C36 12pF IRQ R5 100k

J4 J5 J6 J7 GNDREF

Analog switch has very low digital current, and should be considered as analog component.

J1
1 GNDREF
2 +BATT
3
4 SDA
5 SCL
6

J2
1 SWDIO
2 SWDCLK
3 GNDREF
4 nRESET
5 SWDIO
6 SWDCLK
7 GNDREF

J3
1 +BATT
2
3
4 GNDREF
5
6
7 SCL
8 SDA
9 A
10 B
11 C
12 D
13 E
14 nRESET

C42 10nF
C41 10nF A
C22 10nF B
C21 10nF C
GND

U4 TS5A3359DCUT
6 A   5 B   IN1   IN2   NO0 NO1 NO2   8 VCC   7 COM   4 GND
VCC   COM1   GND
J10 J8 J6   GND 2

U11 TS5A3359DCUT
VCC   COM2   GND
J11 J9 J7   GND 2

U10 TS5A3359DCUT
VCC   COM3   GND
J13 J15 J17   GND 2

U12 TS5A3359DCUT
VCC   COM4   GND
J14 J16 J18   GND 2

U1 ADG849
S2 6 SIG_OUT 5 COM1 4
IN 1 VDD 2 GND 3
COM2
C9 10nF   C28 10nF
VCC GND
C16 0.1uF
VCC GND

U9 ADG849
S2 6 SIG_IN 5 COM3 4
IN 1 VDD 2 GND 3
COM4
C18 10nF   C17 10nF
VCC GND
C21 0.1uF
VCC GND

U2 AD8606ARZ
V_P 8 OUTA 1 OUTB 7 V_N 4
INA_P INA_N INB_P INB_N
R8 20K SIG_OUT VIN
R10 20
+3V0 SIG_OUT GND
C6 0.1uF C5 10uF
+3V0 GND

R1 49.9K R2 49.9K
INB_P +3V0 GND VCC

R5 49.9K R7 49.9K
VDDA +3V0
C7 47nF
SIG_OUT INB_P SIG_IN GND GNDREF

U7 ADP150AUJZ-3.0-R7
VIN OUT 5 EN NC 4 GND
C8 0.1uF
C15 10uF
+3V0 GND
C14 0.1uF
C13 10uF
VCC GND

U8 AP2112K-3.3
VIN VOUT 5 EN GND
C20 10uF
VCC
C19 10uF
+BATT GND

FB2
VDDA VCC

C4 0.1uF
C3 10uF
+3V0 GND

C10 0.01uF
C2 0.1uF
C1 10uF
VDDA GND

U3 AD5933YRSZ-REEL7
9 DVDD 10 AVDD1 11 AVDD2 6 VOUT
12 DGND 13 AGND1 14 AGND2
5 VIN 4 RFB 8 MCLK 16 SCL 15 SDA
R6 20K
MCLK SCL SDA

R13 0 R3 0 R4 0 R9 0 R12 0 R14 0 R16 0 R15 0
GND GNDREF

U6 ASFLMB-16.000MHz-LY-T
4 VDD 3 OUTPUT 1 STANDBY 2 GND
MCLK
C12 15pF/25pF/40pF
GNDREF
FB1
VDD VCC

R11 10K
C11 0.01uF
VDD GNDREF

H4 GNDREF
H3 GNDREF GNDREF
H2
H1

TP3 +3V0
TP2 GND
TP1 VCC

Sheet: /
File: Sensor_module.sch
Title: LunarWSN_Sensor
Size: User   Date: 2020-12-29
KiCad E.D.A. kicad (5.1.8)-1
Rev: V1
Id: 1/1

Title: LunarWSN SlowControl module

SlowControl module is responsible for monitoring internal environment, including battery voltage and temperature

Sheet: /
File: SlowControl.sch
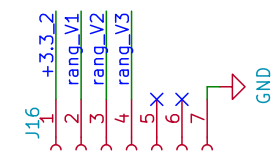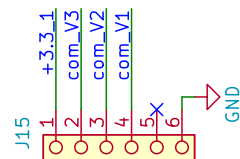
Size: User
Date:
KiCad E.D.A. kicad (5.1.8)-1

Rev:
Id: 1/1

U3 — ADS1115IDGST

U2 — Sparkfun_LSM9DS1_module

U1 — AP2112K-3.3

Temperatures monitoring

Battery voltage monitoring

Reset of MCU — PTS840_GKP_SMTR_LFS

Battery input

Vin

J7

J5

J2

J1

ANT1
AH086M555003-T

ANT1
AH086M555003-T

SC3 SC1 SC2

D3 D1 D2

J3

J1

H4

H3

H2

H1

AE1
A5839

L1
1.2nH

C1
6.5pF

C2
6.5pF

C3
6.5pF

GND

GND

GND

J2

J5
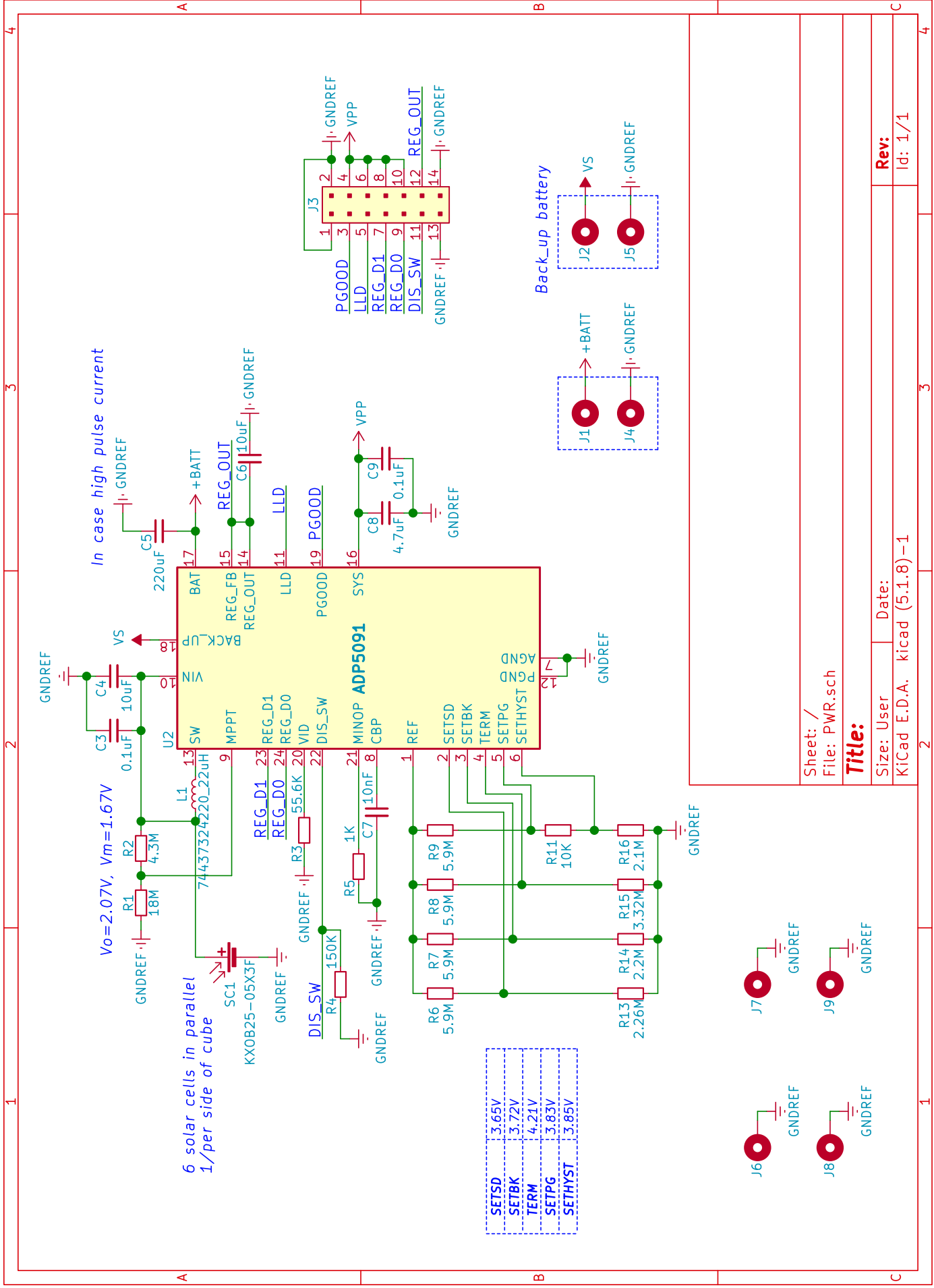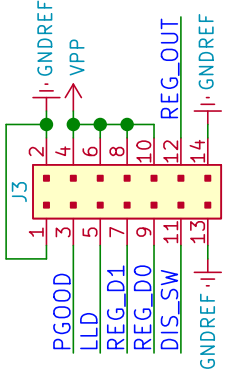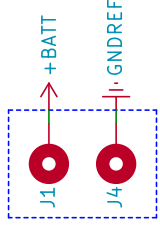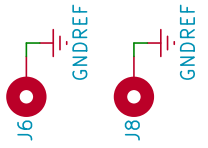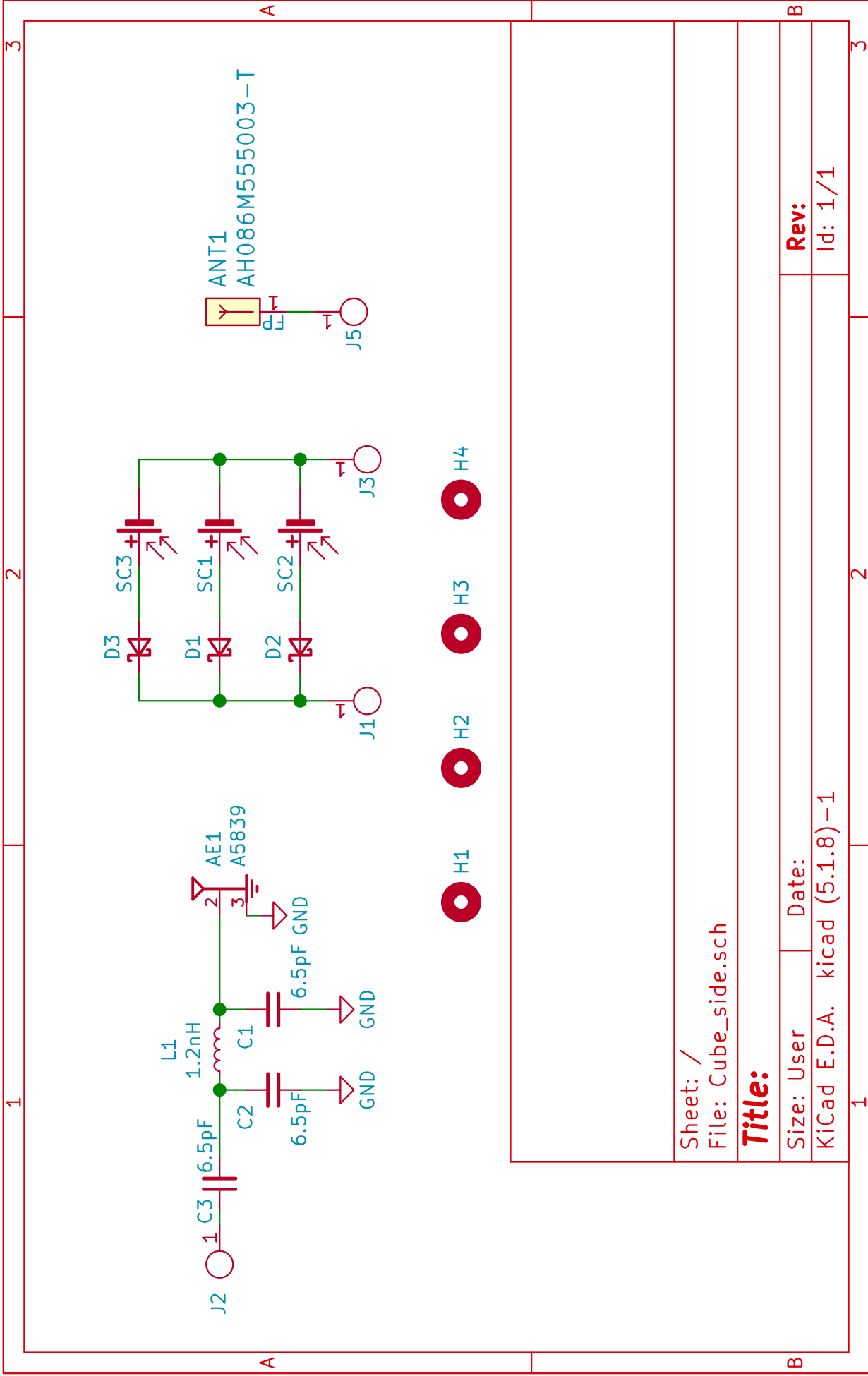
Sheet: /
File: Cube_side.sch
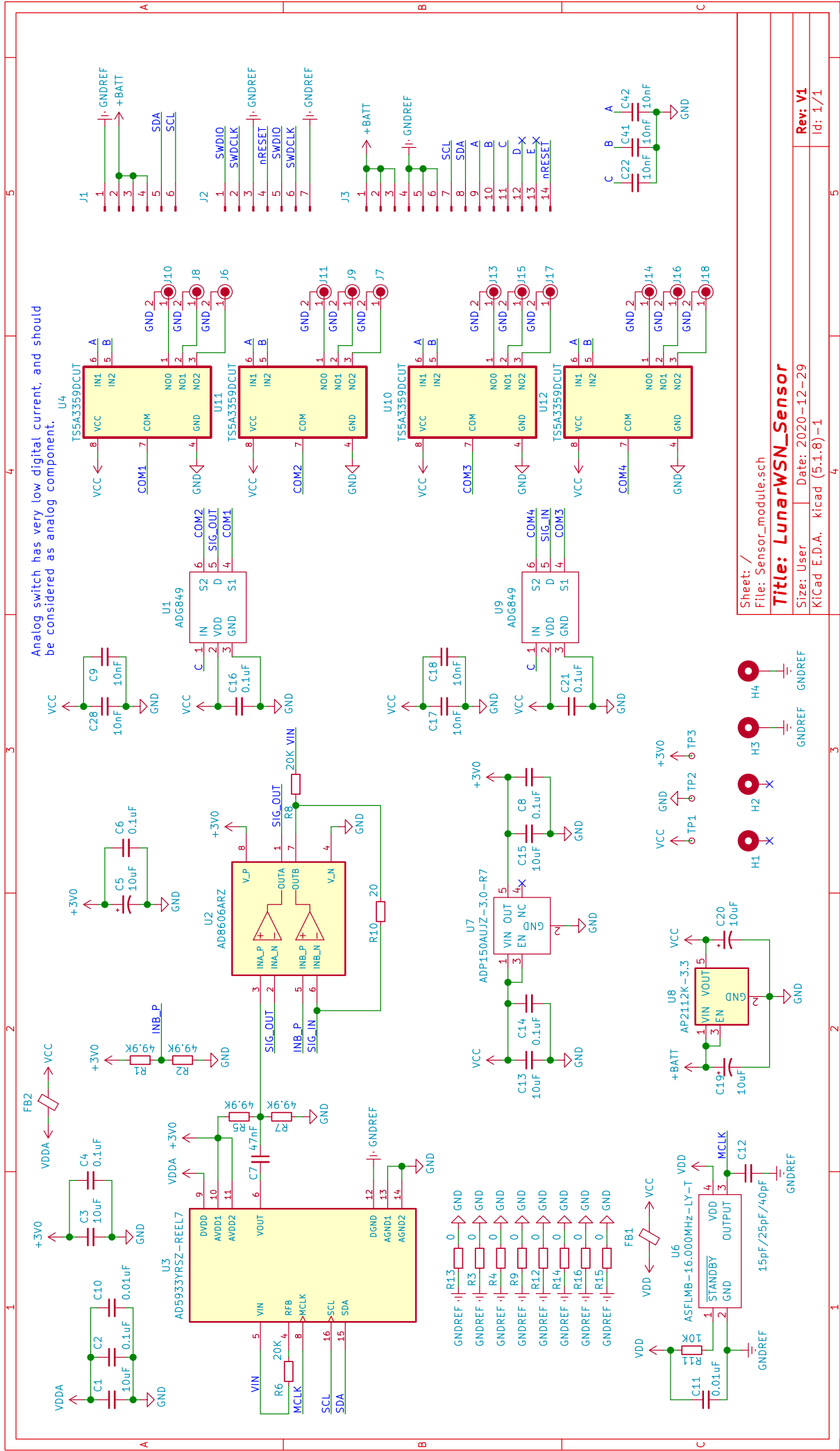
Title:

Size: User   Date:
KiCad E.D.A.   kicad (5.1.8)-1

Rev:

Id: 1/1

Bibliography

[1] *"Space technology research grants program, Lunar surface technology research opportunities appendix,"* NASA, 2020. Available online: `https://nspires.nasaprs.com/external/solicitations/summary.do?solId={0BA38320-8F63-2EAF-D97B-0AB42AF17C35}`

[2] *"The Importance of Lunar Water,"* SPACEREF, 2009. Available online: `http://www.spaceref.com/news/viewnews.html?id=1352`

[3] M. Dille, D. Nuch, S. Gupta, S. McCabe, N. Verzic, T. Fong, and U. Wong, *"PHALANX: Expendable projectile sensor networks for planetary exploration,"* IEEE Aerospace Conference, 2020.

[4] L. Calle, *"Corrosion on mars effects of the mars environment on spacecraft materials,"* NASA Technical Publication 220238, 2019.

[5] *"Technology Horizons: Game-Changing Technologies for the Lunar Architecture,"* The Tauri Group, 2009. Available online: `https://brycetech.com/reports/report-documents/NASA\_Technology\_Horizons\_2009.pdf`

[6] *"Tidmarsh Living Observation,"* Available online: `https://tidmarsh.media.mit.edu/`

[7] K. Pister and J. Kahn and B. Boser, *"Smart dust: wireless networks of millimeter-scale sensor nodes,"* Highlight Article in Electronics Research Laboratory Research Summary, 1999.

[8] J. Manobianco, R.J. Evans, K. Pister, D.M. Manobianco, *"GEMS: A Revolutionary System for Environmental Monitoring,"* Proc. Nanotech 04, pp 422 – 425, 2004.

[9] M. Y. Hariyawan, et al., *"Wireless Sensor Network for Forest Fire Detection,"* TELKOMNIKA, vol/issue: 11(3), 2013.

[10] Magness, R., Plancke, P. *"ESA TEC-E wireless technology dossier, Annex A, an assessment of wireless proximity networks for space applications,"* in: Proceedings of 9th ESA Workshop on Advanced Space Technologies for Robotics and Automation, ASTRA 2006, ESTEC, Noordwijk, The Netherlands, November 28–30, 2006.

[11] Joe Shoer, Rick Stoner, Mason Peck, Zac Manchester, Lorraine Weis, *Exploration Architecture with Quantum Inertial Gravimetry and In-situ ChipSat Sensors*, NIAC Phase I Final Report, April 28, 2015.

[12] John Elliott, Leon Alkalai, *A Discovery-class Lunette mission concept for a lunar geopyhysical network*, 61st International Astronautical Congress 2010, Prague, Czech Republic, September 27 - October 1, 2010.

[13] *LEMS: Lunar Environment Monitoring Station*, Available online: `https://www1.grc.nasa.gov/wp-content/uploads/Lunar\-Environment\ -Monitoring\-Station.pdf`

[14] P. Rodrigues et al., *Space Wireless Sensor Networks for planetary exploration: Node and network architectures*, 2014 NASA/ESA Conference on Adaptive Hardware and Systems (AHS), Leicester, 2014, pp. 180-187, doi: 10.1109/AHS.2014.6880175.

[15] *"LunaH-Map Science,"* Available online: `https://lunahmap.asu.edu/science`

[16] Schultz, P.H. et al., 2010. *"The LCROSS cratering experiment,"* Science 330 (6003), 468–472.

[17] Colaprete A, Schultz P, Heldmann J, Wooden D, Shirley M, Ennico K, Hermalyn B, Marshall W, Ricco A, Elphic RC, Goldstein D, Summy D, Bart GD, Asphaug E, Korycansky D, Landis D, Sollitt L. *"Detection of water in the LCROSS ejecta plume,"* Science. 2010 Oct 22;330(6003):463-8. doi: 10.1126/science.1186986. PMID: 20966242.

[18] *"VIPER Mission Overview,"* NASA, 2020. Available online: `https://www.nasa.gov/viper/overview\#KeyFacts`

[19] *"Water on the moon",* Available online: `https://whyfiles.org/060moons/ourmoon2.html`

[20] *"THE LUNAR INFRARED LASER SPECTROMETER FOR ICE PROSPECTING AND CAVE EXPLORATION,"* Dobrea, E. et al. 2020.

[21] D. Wobschall, *"A Theory of the Complex Dielectric Permittivity of Soil Containing Water: The Semidisperse Model,"* in IEEE Transactions on Geoscience Electronics, vol. 15, no. 1, pp. 49-58, Jan. 1977, doi: 10.1109/TGE.1977.294513.

[22] *"Dielectric Permittivity,"* Available online: `https://soilsensor.com/articles/dielectric-permittivity/`

[23] Reddragon *"Wood Moisture Meter Two Pins Wall Moisture Detector Paper Humidity Tester for Wood Building Material Firewood Moisture Meter Walls Paper Floor (Orange),"* Available online: `https://www.amazon.com/Moisture-Reddragon-Detector-Humidity-Building/dp/B0894STPY2/ref=sr_1_2_sspa?dchild=1&keywords=moisture+detector&qid=1628645943&sr=8-2`

[24] Klein Tools, *"Klein Tools ET140 Pinless Moisture Meter for Non-Destructive Moisture Detection in Drywall, Wood, and Masonry; Detects up to 3/4-Inch Below Surface,"* Available online: `https://www.amazon.com/Klein-Tools-ET140-Non-Destructive-Detection/dp/B07SZX8QXH/ref=sr_1_2?dchild=1&keywords=moisture+detector&qid=1628645986&sr=8-2`

[25] Kremer F, *"Dielectric spectroscopy: Yesterday, today and tomorrow,"* Journal of Non-Crystalline Solids, 305, 1–9 (2000).

[26] M. G. Buehler et al., *"Electrical properties cup (EPC) for characterizing water content of martian and lunar soils,"* 2006 IEEE Aerospace Conference, Big Sky, MT, 2006, pp. 18 pp.-, doi: 10.1109/AERO.2006.1655752.

[27] J. P. Pabari, Y. B. Acharya, U. B. Desai and S. N. Merchant, *"Development of Impedance-Based Miniaturized Wireless Water Ice Sensor for Future Planetary Applications,"* in IEEE Transactions on Instrumentation and Measurement, vol. 61, no. 2, pp. 521-529, Feb. 2012, doi: 10.1109/TIM.2011.2164292.

[28] C.S. Ray, S.T. Reis, S. Sen, J.S. O'Dell, *"JSC-1A lunar soil simulant: Characterization, glass formation, and selected glass properties,"* Journal of Non-Crystalline Solids, Volume 356, Issues 44–49, 2010.

[29] Suresh Seshadri, Keith B. Chin, Martin G. Buehler, and Robert C. Anderson., *"Using Electrical Impedance Spectroscopy to Detect Water in Planetary Regoliths,"* Astrobiology. 781-792. Aug 2008.

[30] J.P. Pabari, Y.B. Acharya, U.B. Desai, S.N. Merchant, *"Concept of wireless sensor network for future in-situ exploration of lunar ice using wireless impedance sensor,"* Advances in Space Research, Volume 52, Issue 2, 2013.

[31] *"nRF52832 Product Specification v1.4",* Available online: `https://infocenter.nordicsemi.com/pdf/nRF52832\_PS\_v1.4.pdf`

[32] *"nRF24L01+ Product Specification v1.0",* Available online: `https://www.nordicsemi.com/-/media/DocLib/Other/Product_Spec/nRF24L01PPSv10.pdf`

[33] *"APS014 APPLICATION NOTE",* Available online: `https://www.decawave.com/wp-content/uploads/2018/08/aps014-antennadelaycalibrationofdw1000-basedproductsandsystems_v1.01.pdf`

[34] *"SKY13416-485LF data sheet",* Available online: `https://www.skyworksinc.com/-/media/SkyWorks/Documents/Products/701-800/SKY13416_485LF_201679I.pdf`

[35] *"AD5933 data sheet",* Available online: `https://www.analog.com/media/en/technical-documentation/data-sheets/AD5933.pdf`

[36] Texas Instruments, *"ADS1115 Product web site",* Available online: `https://www.ti.com/product/ADS1115`

[37] Analog Devices, *"AD5091 Product web site",* Available online: `https://www.analog.com/en/products/ad5391.html`

[38] antenova, *"A5839 data sheet",* Available online: `http://antenova.com/wp-content/uploads/2016/01/Rufa-A5837-A5887-PS-1-2.pdf`

[39] Taiyo Yuden, *"AH086M555003 data sheet",* Available online: `https://media.digikey.com/pdf/Data%20Sheets/Taiyo%20Yuden%20PDFs%20URL%20links/AH086M555003_Char.pdf`

[40] ANYSOLAR Ltd, *"KXOB25_05X3F Product web site",* Available online: `https://www.mouser.com/ProductDetail/Antenova/A5839?qs=b4vKS93X7SyuONuJ58DuXg%3D%3D`

[41] V. Badescu, *"Moon: Prospective Energy and Material Resources,"* 10.1007/978-3-642-03629-3, 2012.

[42] Texas Instruments, *"INA169 Product web site",* Available online: `https://www.ti.com/product/INA169`

[43] *"Acme Analytical Solutions, Deionized Water, Ultrapure, DI Water, 1 Gallon, 3.8 Liters",* Available online: `https://www.amazon.com/Analytical-Solutions-Deionized-Ultrapure-Gallon/dp/B08DL4WHMH/ref=sr_1_5?dchild=1&keywords=type+1+water&qid=1627507732&sr=8-5`

83

[44] *"LMS-1 Lunar Mare Simulant | Fact Sheet",* Available online: `https://sciences.ucf.edu/class/wp-content/uploads/sites/23/2019/02/Spec_LMS-1.pdf`

[45] J. Kuriakose, S. Joshi, R. V. Raju, and A. Kilaru, *"A review on localization in wireless sensor networks,"* in Advances in Signal Processing and Intelligent Recognition Systems. New York, NY, USA: Springer, 2014, pp. 599–610.

[46] A. Svensson, *"Range-based Wireless Sensor Network Localization for Planetary Rovers",* Dissertation, 2020.

[47] Wu. H, et al., *"Real-time localization algorithm for maritime search and rescue wireless sensor network",* Int. J. Distrib. Sens. Netw. 2013, 188–192. 2013.

[48] Patwari, N., Ash, J.N., Kyperountas, S., Hero, A.O., Moses, R.L. and Correal, N.S., *"Locating the nodes: cooperative localization in wireless sensor networks,"* IEEE Signal processing magazine, 22(4), pp.54-69. 2005.

[49] Santra, S., Paet, L.B., Staudinger, E. and Yoshida, K., *"RADIO PROPAGATION MODELLING FOR COORDINATION OF LUNAR MICRO-ROVERS".*

[50] Zhu, Q., Wang, C., Chen, X., Chen, C., Wang, X. and Zhang, C., *"Path loss prediction model of radio propagation over lunar surface,"* In International Conference on High Performance Networking, Computing and Communication Systems, (pp. 556-562). Springer, Berlin, Heidelberg. 2011, May.

[51] Hwu, S., Upanavage, M. and Sham, C., *"Lunar surface propagation modeling and effects on communications,"* In 26th International Communications Satellite Systems Conference (ICSSC). 2008, June.

[52] *"Lunar GPS? NASA Knows How to Help Astronauts Navigate,"* Available online: `https://www.space.com/nasa-developing-lunar-gps-capability.html`

[53] *"Galileo will help Lunar Pathfinder navigate around Moon,"* Available online: `https://www.esa.int/Applications/Navigation/Galileo_will_help_Lunar_Pathfinder_navigate_around_Moon`

[54] *"NASA Explores Upper Limits of Global Navigation Systems for Artemis,"* Available online: `https://www.nasa.gov/feature/goddard/2021/nasa-explores-upper-limits-of-global-navigation-systems-for-artemis`

[55] Batista, A., Gomez, E., Qiao, H. and Schubert, K.E., *"Constellation Design of a Lunar Global Positioning System Using CubeSats and Chip-Scale Atomic Clocks,"* In WorldComp. 2012, April.

[56] Cheng, K.Y., Lui, K.S. and Tam, V., *"Localization in sensor networks with limited number of anchors and clustered placement,"* In 2007 IEEE Wireless Communications and Networking Conference, (pp. 4425-4429). IEEE. 2007, March.

[57] Zhang, B., Fan, J., Dai, G. and Luan, T.H., *"A hybrid localization approach in 3D wireless sensor network,"* International Journal of Distributed Sensor Networks, 11(10), p.692345. 2015.

[58] Pingyuan, C., Fuzhan, Y. and Hutao, C., *"Research on autonomous navigation of lunar rovers for the moon exploration,"* In 2006 IEEE International Conference on Robotics and Biomimetics (pp. 1042-1047). IEEE. 2006, December.

[59] Goldberg, S.B., Maimone, M.W. and Matthies, L., *"Stereo vision and rover navigation software for planetary exploration,"* In Proceedings, IEEE aerospace conference (Vol. 5, pp. 5-5). IEEE. 2002, March.

[60] Sigel, D.A. and Wettergreen, D., *"Star tracker celestial localization system for a lunar rover,"* In 2007 IEEE/RSJ International Conference on Intelligent Robots and Systems (pp. 2851-2856). IEEE. 2007, October.

[61] Broxton, M., Lifton, J., and Paradiso, J.A., *"Localization on the pushpin computing sensor network using spectral graph drawing and mesh relaxation,"* ACM Mobile Computing and Communications Review, January 2006, pp. 1-12.

[62] *"Efficiency of Solar energy harvesting,"* Available online: `https://www.construction21.org/articles/h/efficiency-of-solar-energy-harvesting.html`

[63] Shahmoradi, J., Maxwell, A., Little, S., Bradfield, Q., Bakhtiyarov, S., Roghanchi, P. and Hassanalian, M., *"The Effects of Martian and Lunar Dust on Solar Panel Efficiency and a Proposed Solution,"* In AIAA Scitech 2020 Forum (p. 1550). 2020.

[64] Walton, O.R., *"Adhesion of lunar dust,"* 2007.

[65] *"Thermal Systems,"* Available online: `https://rps.nasa.gov/power-and-thermal-systems/thermal-systems/light-weight-radioisotope-heater-unit/`

[66] Valle Lozano, A., *"Development of a Lunar Regolith Thermal Energy Storage Model for a Lunar Outpost,"* 2016.

[67] Serra, P. and González Cinca, R., *"Thermoelectric generators for long duration lunar missions,"* In 8th European Conference for Aeronautics and Space Science (EUCASS): papers (pp. 1-14). 2019.

[68] Nejad, A.R., Nejad, A.R., Abedi, M.E. and Nejad, A.R., *"Production of electrical power in very extreme-temperature environmental conditions: A new implementation of thermoelectric generators,"* In 2017 IEEE 6th International Conference on Renewable Energy Research and Applications (ICRERA) (pp. 468-472). IEEE. 2017, November.

[69] *"Plutonium-238 Production for Space Exploration,"* Available online: `https://www.acs.org/content/acs/en/education/whatischemistry/landmarks/plutonium-238-production.html`

[70] NASA RPS, *"What is Plutonium-238?"*

[71] Vaniman, D., Reedy, R., Heiken, G., Olhoeft, G. and Mendell, W., *"The lunar environment,"* The lunar Sourcebook, CUP, pp.27-60. 1991.

[72] Swami, A., Zhao, Q., Hong, Y.W. and Tong, L. eds., *"Wireless sensor networks: signal processing and communications perspectives,"* John Wiley & Sons. 2007.

[73] *"LoRa,"* Available online: `https://en.wikipedia.org/wiki/LoRa`

[74] Semtech, *"SX1276/77/78/79 datasheet,"* Available online: `https://www.mouser.com/datasheet/2/761/sx1276-1278113.pdf`

[75] Ho, T.M., Baturkin, V., Grimm, C., Grundmann, J.T., Hobbie, C., Ksenik, E., Lange, C., Sasaki, K., Schlotterer, M., Talapina, M. and Termtanasombat, N., *"MASCOT—the mobile asteroid surface scout onboard the HAYABUSA2 mission,"* Space Science Reviews, 208(1), pp.339-374. 2017.

[76] *"'Hedgehog' Robots Hop, Tumble in Microgravity,"* Available online: `https://www.jpl.nasa.gov/news/hedgehog-robots-hop-tumble-in-microgravity`

[77] J. W. Romanishin, K. Gilpin, and D. Rus, *"M-blocks: momentum-driven, magnetic modular robots,"* in Proceedings of the 26th IEEE/RSJ International Conference on Intelligent Robots and Systems (IROS '13), pp. 4288–4295, IEEE, Tokyo, Japan, November 2013.

[78] J. W. Romanishin, K. Gilpin, S. Claici, and D. Rus, *"3D MBlocks: self-reconfiguring robots capable of locomotion via pivoting in three dimensions,"* in Proceedings of the IEEE International Conference on Robotics and Automation (ICRA'15), pp. 1925–1932, Seattle, Wash, USA, May 2015.

[79] Watanabe, S.I., Tsuda, Y., Yoshikawa, M., Tanaka, S., Saiki, T. and Nakazawa, S., *"Hayabusa2 mission overview,"* Space Science Reviews, 208(1), pp.3-16. 2017.

[80] *"Legged Robots Do Surprisingly Well in Low Gravity,"* Available online: `https://spectrum.ieee.org/automaton/robotics/space-robots/legged-robots-surprisingly-well-low-gravity`

[81] B. Wilcox, T. Litwin, J. Biesiadecki, J. Matthews, M. Heverly, J. Morrison, J. Townsend, N. Ahmad, A. Sirota, and B. Cooper, *"Athlete: A cargo handling and manipulation robot for the moon,"* in Journal of Field Robotics, vol. 24, 2007, pp. 421–434.

[82] T. Bretl, S. Rock, J. Latombe, B. Kennedy, and H. Aghazarian, *"Free-climbing with a multi-use robot,"* in Experimental Robotics, vol. IX, 2006, pp. 449–458.

[83] S. Howe, R. O'Brien, N. Jerred, S. Cooley, J. Crepeau, S. Hansen, and A. Klein, *"The mars hopper: A radioisotope powered, impulse driven, long-range, long-lived mobile platform for exploration of mars,"* in Concepts and Approaches for Mars Exploration, 2012.

[84] Schroeder, G., *"NASA's Ingenuity Mars Helicopter: The first attempt at powered flight on another world,"* American Scientist, 108(6), pp.330-331. 2020.

[85] T. A. Liljeb¨ack, P. and K. Fossum, *"Serpentine robots for planetary exploration (serpex),"* in SINTEF Report, 2014.

[86] Fa, W., *"Exploration Subsurface Structure of the Moon: Potential Scientific Return from a Ground Penetrating Radar,"* In Lunar and Planetary Science Conference (No. 1659, p. 1274). 2012, March.

[87] Li, C. et al. *"Te Moon's farside shallow subsurface structure unveiled by Chang'e-4 lunar penetrating radar,"* Sci. Adv. 6, eaay6898 (2020).

[88] *"How to select GPR antenna frequency?"* Available online: `https://www.sensoft.ca/gpr/antenna-frequency/`

[89] Paul O. Hayne, et al., *"New Approaches to Lunar Ice Detection and Mapping,"* 2014, Apr.

[90] Acconeer AB, *"A111 product web site,"* Available online: `https://www.digikey.com/en/products/detail/acconeer-ab/A111-001-T-R/10056085`

[91] Acconeer AB, *"XR112 product web site,"* Available online: `https://www.digikey.com/en/products/detail/acconeer-ab/XR112/9356271`

[92] Texas Instruments, *"IWR1843 product web site,"* Available online: `https://www.digikey.com/en/products/detail/texas-instruments/IWR1843AQGABLR/10711016`

[93] Zhang, S., Wimmer-Schweingruber, R.F., Yu, J., Wang, C., Fu, Q., Zou, Y., Sun, Y., Wang, C., Hou, D., Böttcher, S.I. and Burmeister, S., *"First measurements of the radiation dose on the lunar surface,"* Science Advances, 6(39), p.eaaz1334. 2020.

[94] Keller, O.; Benoit, M.; Müller, A.; Schmeling, S. *"Smartphone and Tablet-Based Sensing of Environmental Radioactivity: Mobile Low-Cost Measurements for Monitoring, Citizen Science, and Educational Purposes,"* Sensors 2019, 19, 4264.

[95] Keller, O., Schmeling, S., Müller, A. and Benoit, M., *"iPadPix—A novel educational tool to visualise radioactivity measured by a hybrid pixel detector,"* Journal of Instrumentation, 11(11), p.C11032. 2016.

[96] Poikela, T., Plosila, J., Westerlund, T., Campbell, M., De Gaspari, M., Llopart, X., Gromov, V., Kluit, R., Van Beuzekom, M., Zappon, F. and Zivkovic, V., *"Timepix3: a 65K channel hybrid pixel readout chip with simultaneous ToA/ToT and sparse readout,"* Journal of instrumentation, 9(05), p.C05013. 2014.

[97] Saunders, D.M., *"The Timepix3 Telescope for LHCb Upgrade RD 1 measurements,"* PoS, p.1186. 2017

[98] Akiba, K., van Beuzekom, M., Boterenbrood, H., Buchanan, E., Buytaert, J., Byczynski, W., Vidal, X.C., Collins, P., Dall'Occo, E., Suárez, A.D. and Dumps, R., *"LHCb VELO Timepix3 telescope,"* Journal of Instrumentation, 14(05), p.P05026. 2019.

[99] Sopczak, A., *"Timepix3 Luminosity Determination of 13-TeV Proton–Proton Collisions at the ATLAS Experiment,"* IEEE Transactions on Nuclear Science, 67(4), pp.609-616. 2020.

[100] Stoffle, N., Pinsky, L., Kroupa, M., Hoang, S., Idarraga, J., Amberboy, C., Rios, R., Hauss, J., Keller, J., Bahadori, A. and Semones, E., *"Timepix-based radiation environment monitor measurements aboard the International Space Station,"*

Nuclear Instruments and Methods in Physics Research Section A: Accelerators, Spectrometers, Detectors and Associated Equipment, 782, pp.143-148. 2015

[101] Akiba, K., Artuso, M., Badman, R., Borgia, A., Bates, R., Bayer, F., Van Beuzekom, M., Buytaert, J., Cabruja, E., Campbell, M. and Collins, P., *"Charged particle tracking with the Timepix ASIC,"* Nuclear Instruments and Methods in Physics Research Section A: Accelerators, Spectrometers, Detectors and Associated Equipment, 661(1), pp.31-49. 2012.

[102] *"3D Charged Particle Tracking"* Available online: `https://medipix.web.cern.ch/3d-charged-particle-tracking`

[103] Jakubek, J. and Uher, J., *"Fast neutron detector based on TimePix pixel device with micrometer spatial resolution,"* in 2009 IEEE Nuclear Science Symposium Conference Record (NSS/MIC) (pp. 1113-1116). IEEE. 2009, October.

[104] Yamada, R., *"The description of Apollo Seismic Experiments,"* Tokyo: Japan Aerospace Exploration Agency. 2013.

[105] Latham, G., Ewing, M., Dorman, J., Nakamura, Y., Press, F., Toksőz, N., Sutton, G., Duennebier, F. and Lammlein, D., *"Lunar structure and dynamics-results from the Apollo passive seismic experiment,"* The Moon, 7(3), pp.396-421. 1973.

[106] Neal, C.R., *"The Importance of Establishing a Global Lunar Seismic Network,"* In Space Resources Roundtable VII: LEAG Conference on Lunar Exploration (Vol. 1287, p. 70). 2005, October.

[107] Board, S.S. and National Research Council, *"The scientific context for exploration of the Moon,"* National Academies Press. 2007.

[108] Mougenot, D., *"How digital sensors compare to geophones?"* In SEG Technical Program Expanded Abstracts 2004 (pp. 5-8). Society of Exploration Geophysicists. 2004.

[109] Analog Devices, *"ADXL355 product web site,"* Available online: `https://www.analog.com/en/products/adxl355.html`

[110] Suhas, E.P., *"Design and development of MEMS based sensor for lunar seismometer."*

[111] Novotny. P, *"Seismic sensors in PACMAN,"* in 1st PACMAN workshop. CERN. 2015, February.

[112] Moushtakim, B., Islam, M. and Rubieyat, B.A., *"Earthquake Vs. Moonquake: A Review,"* World Scientific News, 100, pp.1-15. 2018.

[113] *"Quake (natural phenomenon),"* Wikipedia.

[114] Li, S., Lucey, P.G., Milliken, R.E., Hayne, P.O., Fisher, E., Williams, J.P., Hurley, D.M. and Elphic, R.C., *"Direct evidence of surface exposed water ice in the lunar polar regions,"* Proceedings of the National Academy of Sciences, 115(36), pp.8907-8912. 2018.

[115] *"Inside Dark, Polar Moon Craters, Water Not as Invincible as Expected, Scientists Argue,"* `https://www.nasa.gov/feature/goddard/2019/inside-dark-polar-moon-craters-water-not-as-invincible-as-expected-scientists-arg`

[116] Nurge, M.A., *"In situ dielectric spectroscopy for water detection on the lunar surface,"* Planetary and Space Science, 65(1), pp.76-82. 2012.

[117] *"LOWER NOISE. SUPERIOR PERFORMANCE. INTRODUCING THE OPTICAL SEISMOMETER,"* Available online: `http://siaudioseismic.com/`

[118] Weber, R.C., DellaGiustina, D., Bailey, S., Avenson, B., Bray, V.J., Otterbacher, S., Burke, K.N., Schmerr, N.C., Siegler, M., Zacny, K. and Marusiak, A.G., *"Optical seismometer for the Lunar Geophysical Network,"* In AGU Fall Meeting 2019. AGU. 2019, December.

[119] Huang, H., Agafonov, V. and Yu, H., *"Molecular electric transducers as motion sensors: A review,"* Sensors, 13(4), pp.4581-4597. 2013.

[120] *"Nanomaterial turns radiation directly into electricity,"* Available online: `https://www.newscientist.com/article/dn13545-nanomaterial-turns-radiation-directly-into-electricity/`

[121] *"MELLTT: Multifunctional Expandable Lunar Lightweight Tall Tower"* Available online: `http://bigidea.nianet.org/wp-content/uploads/2021/01/2020-BIG-Idea-Team-Digital-Poster_MIT.pdf`

[122] Paudel, A., *"Energy harvesting from solar wind and galactic cosmic rays,"* Journal of Energy Research and Environmental Technology, 1, pp.33-36. 2014.

[123] Vanamala, U.M. and Nidamarty, L.P., *"Galactic Cosmic Energy-A Novel Mode of Energy Harvesting,"* In International Conference on Emerging Trends in Engineering (ICETE) (pp. 458-465). Springer, Cham. 2020.